Bioactive Materials 45 (2025) 417–433

Contents lists available at ScienceDirect

Bioactive Materials

journal homepage: www.keaipublishing.com/en/journals/bioactive-materials

In situ magnetic-field-assisted bioprinting process using magnetorheological bioink to obtain engineered muscle constructs

Hanjun Hwangbo [a,b,1], SooJung Chae [a,1], Dongryeol Ryu [c], GeunHyung Kim [a,b,d,*]

[a] Department of Precision Medicine, Sungkyunkwan University School of Medicine (SKKU-SOM), Suwon, 16419, Republic of Korea
[b] Institute of Quantum Biophysics, Department of Biophysics, Sungkyunkwan University, Suwon, Gyeonggi-do, 16419, Republic of Korea
[c] Department of Biomedical Science and Engineering, Gwangju Institute of Science and Technology, Gwangju, Republic of Korea
[d] Biomedical Institute for Convergence at SKKU (BICS), Sungkyunkwan University, Suwon, 16419, Republic of Korea

ARTICLE INFO

Keywords:
Anisotropic tissue
Magnetorheological bioink
VML therapeutics
Magnetic field
Muscle regeneration

ABSTRACT

Tissue-engineered anisotropic cell constructs are promising candidates for treating volumetric muscle loss (VML). However, achieving successful cell alignment within macroscale 3D cell constructs for skeletal muscle tissue regeneration remains challenging, owing to difficulties in controlling cell arrangement within a low-viscosity hydrogel. Herein, we propose the concept of a magnetorheological bioink to manipulate the cellular arrangement within a low-viscosity hydrogel. This bioink consisted of gelatin methacrylate (GelMA), iron oxide nanoparticles, and human adipose stem cells (hASCs). The cell arrangement is regulated by the responsiveness of iron oxide nanoparticles to external magnetic fields. A bioprinting process using ring magnets was developed for *in situ* bioprinting, resulting in well-aligned 3D cell structures and enhanced mechanotransduction effects on hASCs. *In vitro* analyses revealed upregulation of cellular activities, including myogenic-related gene expression, in hASCs. When implanted into a VML mouse model, the bioconstructs improved muscle functionality and regeneration, validating the effectiveness of the proposed approach.

1. Introduction

In situ bioprinting systems, first conceptualized by Campbell et al., represent a groundbreaking advancement in the field of regenerative medicine, merging the precision of 3D printing with the biological complexity of tissue engineering [1]. Unlike conventional methods for the delivery of therapeutics, in which bioprinters create tissue constructs in a laboratory (*in vitro*) for later implantation, *in situ* bioprinters fabricate bioconstructs directly at the injury site using bioinks composed of living cells and biomaterials [2]. This innovative approach facilitates enhanced integration with native tissues, lowers the risk of infection and rejection, allows precise customization of cell constructs, and reduces the need for multiple surgical interventions [3]. For example, multi-barrel extrusion-based bioprinting successfully deposited autologous dermal fibroblasts and epidermal keratinocytes onto skin defect sites in porcine models, demonstrating significant wound-healing capabilities [4]. *In situ* bioprinting can be challenging due to the need for a large operational space and a sizable wound, which increases the risk of infection and delays healing. However, combining minimally invasive surgery with endoscope-assisted *in situ* bioprinting allows for precise bioprinting in smaller wound areas, reducing infection risks and promoting faster healing.

Although *in situ* bioprinters developed in recent years offer distinct advantages, the biophysical functionality of *in situ* bioprinted structures remains unclear. This is primarily because most *in situ* printing systems can only deliver a mixture of cells and bioactive materials to the damaged sites. Consequently, the resulting tissue constructs often lack the necessary complexity and functionality, impeding effective regeneration and integration with the host tissue. To overcome this limitation, integrating *in situ* bioprinting technologies with dynamic stimuli such as mechanical [5], electrical [6–9], and topographical stimulation [10–13]—during the deposition process can create appropriate niches for printed cell constructs. This integration promotes better integration with the host tissue and accelerates the regenerative process [6,7,14].

Previously, we investigated an *in situ* stimulation-assisted bioprinting strategy by applying an electric field during bioink extrusion. This approach significantly enhanced cellular activities and provided effective therapeutics for VML defects in mice [6,7]. Despite these

* Corresponding author. Department of Precision Medicine, Sungkyunkwan University School of Medicine (SKKU-SOM), Suwon, 16419, Republic of Korea.
E-mail address: gkimbme@skku.edu (G. Kim).
[1] The authors contributed equally.

https://doi.org/10.1016/j.bioactmat.2024.11.035
Received 21 September 2024; Received in revised form 17 November 2024; Accepted 28 November 2024
Available online 3 December 2024

advantages, complex equipment, intricate printing setups, and narrow printing parameters limit the applicability of the system for *in situ* bioprinting. Additionally, we explored the use of a blade-modified nozzle for mechanical stimulation, which was aimed at enhancing cell alignment and promoting tissue regeneration [5]. However, this method faces a significant limitation when attempting to integrate it with *in situ* bioprinting. The blade-modified nozzle requires a rigid printing stage to apply consistent mechanical force, which complicates the printing process. Consequently, there is a need for simple yet effective strategies that can induce physical stimulation of cells during the *in situ* bioprinting process, thereby ensuring effective tissue regeneration.

Recently, the application of magnetic fields (M-fields) to induce mechanotransduction responses in cells has gained attention in muscle tissue engineering [15]. *In vitro* studies have suggested that cellular cultures stimulated with an M-field can achieve positive cellular alignment and myogenesis *via* phosphorylation of myosin light-chain kinase (MLCK), a process that is influenced by the activation of key mechanosensitive pathways. When exposed to M-fields, cells are known to activate focal adhesion kinase (FAK) and integrins, which help mediate the mechanical coupling between the extracellular matrix and the cytoskeleton [16,17]. This mechanotransduction leads to the phosphorylation of MLCK, resulting in alterations in actin-myosin contractility that promote cellular alignment and differentiation [15]. Among the various magnetic particles available, iron oxide micro/nanoparticles are commonly used to induce mechanotransduction and phosphorylation of MLCK. When exposed to an external magnetic field, these nanoparticles exert mechanical forces on the cells, influencing their morphology and behavior by interacting with the extracellular matrix and cytoskeleton. Additionally, the magnetic field induces alignment of the iron oxide particles in its direction, creating a topographical cue that further guides cellular orientation [18]. This combination of mechanical force and topographical guidance promotes cellular alignment and activates mechanotransduction processes. Wang et al. incorporated iron oxides into electrospun nanofibers to develop an injectable hydrogel that could be manipulated by controlling the M-field [19]. The *in vitro* results using C2C12 cells demonstrated that the cells could align according to the direction of the M-field. Notably, injection of this hydrogel into a VML defect in rats, followed by exposure to an M-field, resulted in alignment of the nanofibers and positive myofiber formation.

Recent research underscore the effectiveness of GelMA-based and composite hydrogels in osteochondral regeneration. For instance, a dynamic GelMA bioink that combines dopamine-functionalized GelMA with β cyclodextrin crosslinking creates a tunable modulus, increased mechanical strength, and enhanced cell adhesion, making it ideal for constructing heterogeneous cell-laden layers with chondrogenic and osteogenic factors that simulate osteochondral environments [20]. Moreover, a recent study has demonstrated a double-layered scaffold containing Mg^{2+} and deferoxamine (DFO) to support site-specific osteochondral regeneration [21]. The scaffold consists of an upper hydrogel layer made of GelMA and hyaluronic acid with small pores, optimized for cartilage regeneration, and a bottom cryogel layer, concentrated GelMA and magnesium carbonate hydroxide (MCH), designed with interconnected macropores for the bone region. The scaffold demonstrated superior regenerative effects in a rabbit trochlea model with osteochondral defects, outperforming scaffolds containing only Mg^{2+} or DFO.

Iron oxide particles are FDA-approved and widely used in biomedical research due to their favorable properties such as biocompatibility, chemical stability, and magnetic properties (Supplementary Table S1) [22]. Previous studies have demonstrated that these particles exhibit minimal cytotoxicity in various *in vivo* models and *in vitro* experiments with several cell types including rat pheochromocytoma (PC12) and human lung adenocarcinoma epithelial cell line (A549). However, the cellular outcomes can vary depending on their size and concentration of iron oxide particles. Generally, above certain threshold concentrations, the particles increase cytotoxicity, reducing cellular activity and elevating reactive oxygen species levels [23], which can ultimately lead to cell apoptosis [24,25]. Conversely, at lower concentrations coupled with M-field stimulation, iron oxide particles demonstrate biocompatibility. Moreover, a study by Chang and colleagues indicated that after 9 weeks, iron oxide/gelatin hydrogel in the gastrocnemius muscles of rats was completely metabolized out of the host through excretion [26]. More importantly, H&E staining of various tissues, including the heart, liver, spleen, lungs, and kidneys, showed no detectable inflammation or defects, indicating the biocompatible characteristics of iron oxide particles.

Given their biocompatibility, iron oxides have been widely utilized in tissue engineering applications for various tissues (Supplementary Table S2). Iron oxide particles are more advantageous over manganese oxide and cobalt oxide due to their higher magnetic properties, particularly their superior saturation magnetization [27–29]. This enhanced magnetic strength, along with their well-established biocompatibility and widespread use in biomedical applications, makes iron oxide a more effective choice for controlling cellular alignment and promoting tissue regeneration. When exposed to a magnetic field, iron oxide particles exert mechanical forces on cells by interacting with the extracellular matrix and cytoskeleton, activating mechanotransduction pathways that promote cellular alignment and differentiation [15]. For example, PCL-based composites loaded with iron oxide have demonstrated enhanced osteogenesis-related gene expression of Wharton's Jelly MSCs [30]. Moreover, Wang et al. have explored the potential of iron oxide for muscle tissue regeneration [19]. The iron oxide containing magnetic fiber was mixed with GelMA and static M-field stimulation was applied to induce the cellular alignment of C2C12. Additionally, when the GelMA formulation was injected into a VML defect in rats, it resulted in upregulated myogenic activities of C2C12 and improved muscle functionality *in vivo*. Moreover, a recent study utilized hydroxyapatite nanorods containing iron oxides (MagHA) within a bioink composed of GelMA and acrylate β-cyclodextrin to create multileveled gradients in composition, mechanics, and magnetism, targeting osteochondral regeneration [31]. Under an external magnetic field, MagHA generated a continuous gradient resembling the transition from superficial to subchondral zones in native osteochondral tissue. This adaptable composite hydrogel facilitates cell infiltration and supports site-specific differentiation, creating an ideal environment for osteochondral defect repair.

Based on our understanding of the positive cellular effects of M-fields and *in situ* alignment strategies, we formulated a magnetic bioink by incorporating nanosized iron oxides into hASCs-laden GelMA hydrogel. During bioink extrusion, ring-shaped magnets were positioned on a glass nozzle to generate an M-field parallel to the bioink flow direction. Various parameters, including the M-field distribution controlled by the number of magnets and sizes of iron oxide particles, were manipulated to achieve optimal alignment of magnetic particles within the bioink, thereby enhancing cellular activities. After selecting the appropriate printing parameters, we evaluated the *in situ* M-field effects on hASCs by comparing three constructs: an *in situ* M-field bioprinted construct with iron oxide, a normally bioprinted construct with iron oxide, and a normally bioprinted construct without iron oxide. *In vitro* cellular results indicated that several cellular activities, including the expression of myogenic-related genes, were significantly enhanced in the M-field assisted bioprinted structure compared with the other constructs. Furthermore, implantation of the M-field-assisted cell construct into a VML mouse model resulted in significant improvements in functionality and muscle regeneration compared with other bioconstructs.

2. Experimental section

2.1. Methacrylation process of gelatin

The methacrylation of gelatin was performed following a previously established procedure [32]. In summary, gelatin (Sigma Aldrich, USA)

sourced from porcine skin was dissolved in phosphate-buffered saline (PBS) at a concentration of 10 % (w/v). Methacrylic anhydride (Sigma Aldrich, USA) was slowly added while stirring continuously at 50 °C. After 2 h, the GelMA underwent dialysis in distilled water using dialysis tubing at 40 °C for 7 d to eliminate any residual methacrylic anhydride. Subsequently, GelMA was freeze-dried for further use.

2.2. Formulation and characterization of magnetorheological bioink

To formulate magnetically active bioink, the freeze-dried GelMA was dissolved in distilled water at 10 wt%. Additionally, sterilized iron oxide particles [Iron(III) oxide; Sigma Aldrich, USA] were added to the 10 wt% GelMA solution in 400 ng mL^{-1} concentration. To prevent aggregation of iron oxide particles, the solution underwent sonification as highlighted in Supplementary Fig. S1. Subsequently, 10 × DMEM solution containing 1 % (w/v) of lithium phenyl-2,4,6-trimethylbenzoylphosphinate (LAP; Sigma–Aldrich, USA) and 2 × 10^7 cells•mL^{-1} hASCs (PT-5006; Lonza, Basel, Switzerland) was added to the solution in 1:1 ratio to formulate magnetically active bioink consisting of 5 wt% GelMA, 200 ng mL^{-1}, 0.5 % (w/v) LAP, and 1 × 10^7 cells•mL^{-1} hASCs.

To assess the rheological properties of the magnetorheological bioinks, a rotational rheometer (Bohlin Gemini HR Nano; Malvern Instruments, UK) was utilized to measure storage modulus (G') and complex viscosity (η*) using temperature sweep (4–32 °C) and a parallel geometry (diameter: 40 mm, gap: 1 mm). Additionally, to provide M-field during rheological evaluation, a neodymium ring (inner diameter = 6.8 mm, outer diameter = 30 mm, and height = 5.2 mm) magnet was placed on the rotating plate.

2.3. Fabrication of iron oxide-incorporated GelMA bioconstructs using in situ M-field assisted bioprinting

To conduct *in situ* M-field assisted bioprinting, a three-axis printing system (DTR3-2210 T-SG; DASA Robot, South Korea) coupled with a dispensing system (AD-3000C; Ugin-tech, South Korea) and UV spot head (LGA-20562, Limtekeu, Incheon, South Korea), and controller (LS-20, Limtekeu, Incheon, South Korea) was used. In addition, the nozzle was modified with light-permeable glass capillaries with an inner diameter of 500 μm (Hirschmann, Eberstadt, Germany) to conduct *in situ* photo-crosslinking. Moreover, three neodymium magnets (inner diameter = 6.8 mm, outer diameter = 30 mm, and height = 5.2 mm) were stacked and positioned around the modified nozzle to provide simultaneous M-field during the extrusion of the magnetically active bioink. The following printing parameters including barrel temperature (10 °C), nozzle moving speed (10 mm s^{-1}), UV dose (~800 mJ cm^{-1}), and pneumatic pressure (100 kPa) were utilized. The magnetic flux distribution around the nozzle was assessed using finite element method magnetics (FEMM) software.

The control group, G was fabricated *via* extruding hASCs (1 × 10^7 cells•mL^{-1}) bearing GelMA using *in situ* photo-crosslinking mechanism [14], whereas GIO was obtained by extruding iron oxide (200 ng mL^{-1})/hASCs bioink (1 × 10^7 cells•mL^{-1}) bearing bioink using *in situ* photo-crosslinking method without the placement of neodymium magnets.

A digital camera connected to an optical microscope (BX FM-32; Olympus, Tokyo, Japan) and scanning electron microscope (SNE-3000M, SEC, Inc., South Korea) was utilized to characterize the morphology of the iron oxide particles and bioconstructs. Regarding energy-dispersive spectroscopy (EDS) analysis, JSM7000F (Jeol, Akishima, Japan) was used for mapping and imaging. ImageJ software (National Institutes of Health, Bethesda, MD, USA).

2.4. In vitro cell culture and activities

The cell-laden bioconstructs were placed in 6-well cell culture plate and cultured in growth media comprised of low-glucose DMEM (DMEM-LG; Sigma-Aldrich, USA), 10 % fetal bovine serum (FBS; Biowest, France) and 1 % penicillin/streptomycin (PS; Gibco, USA). To induce myogenesis of hASCs, after 7 d of culture, the bioconstructs were cultured in myogenic media comprised of DMEM-LG containing 10 % FBS, 5 % horse serum, 0.1 μM dexamethasone, 50 μM hydrocortisone, and 1 % PS. The medium was changed every 2 d and the bioconstructs were cultured in 5 % CO_2 at 37 °C.

The cell proliferation rate of hASCs was monitored by conducted MTT [3-(4,5-dimethylthiazol-2-yl)-2,5-diphenyltetrazolium bromide] assay (Cell Proliferation Kit I; Boehringer Mannheim, Mannheim, Germany). The bioconstructs were reacted with 0.5 mg mL^{-1} MTT solution for 4 h at 37 °C. The formazan crystals formed were dissolved using a solubilization solution and the optical density was measured at 570 nm using a microplate reader (Epoch; BioTek, South Korea).

To evaluate the cell viability of hASCs processed using *in situ* M-field assisted bioprinting, the bioconstructs were examined for live/dead assay. Briefly, the printed structures were subjected to staining with a 0.15 mM calcein AM/2 mM ethidium homodimer-1 solution (Invitrogen, USA) and then incubated in a 5 % CO_2 atmosphere at 37 °C for 1 h. Subsequently, the stained cells were visualized using a confocal microscope (LSM 700; Carl Zeiss, Germany), and the number of green and red cells was quantified using ImageJ software to determine cell viability. Additionally, the morphology of cells including cell nuclei and actin filaments (F-actin) were visualized using DAPI/phalloidin staining. The cells were fixated using with 3.8 % paraformaldehyde (252549; Sigma Aldrich St Louis, USA) for 1 h at 37 °C and permeabilized with 0.1 % Triton X-100 for 20 min at 37 °C. Then, the cells within bioconstruct were stained using 4′,6-diamidino-2-phenylindole (DAPI; blue) (diluted 1:100 in PBS; Invitrogen) and Alexa Fluor 594 phalloidin (red) (diluted 1:100 in PBS; Invitrogen) staining solution. The stained nuclei and F-actin were visualized using a confocal microscope. Subsequently, ImageJ software was utilized for quantitative analysis including cell aspect ratio and orientation factor.

2.5. Immunofluorescent staining

To conduct immunofluorescent staining of the hASCs, the bioconstructs were rinsed using PBS three times, followed by cell fixation using 3.8 % paraformaldehyde solution for 2 h at 37 °C. Then the cells were permeabilized using 2 % Triton X-100 solution and treated with 2 % bovine serum albumin (BSA; Sigma-Aldrich, USA) for 2 h at 37 °C. Then, the bioconstructs were treated with mouse anti-piezo1 (5 μg mL^{-1} in PBS; Invitrogen), mouse anti-MF20 (5 μg mL^{-1} in PBS; Developmental Studies Hybridoma Bank, USA), rabbit anti-α-actinin (5 μg mL^{-1} in PBS; PA5-27863; Invitrogen) primary antibodies overnight at 4 °C, followed by staining with Alexa Fluor 488- and 594-conjugated secondary antibodies (1:50 in PBS; Invitrogen) for 1 h at 37 °C. Finally, the nuclei were counterstained using DAPI (5 μM in PBS) for 5 min at 37 °C.

2.6. qRT-PCR test

For the evaluation of gene expression in the bioprinted structures, quantitative reverse transcription PCR (qRT-PCR) was conducted. Initially, total RNA was extracted from the samples using TRIzol® Reagent (ThermoFisher Scientific, USA). Then, the isolated RNA, ensured to be RNase-/DNase-free, underwent reverse transcription utilizing the ReverTraAce qPCR RT Master Mix (Toyobo Co., Ltd., Japan), leading to the generation of cDNA. This synthesized cDNA served as the template for qRT-PCR analysis, employing Thunderbird® SYBR® qPCR mix (Toyobo Co., Ltd., Japan) and a StepOnePlus PCR system (Applied Biosystems, USA) to measure cycle threshold (Ct) values. The obtained values were normalized to the glyceraldehyde 3-phosphate dehydrogenase (GAPDH) housekeeping gene to get the ΔCt values. Additionally, regarding gel electrophoresis results, the PCR products after performing 30 cycles of qRT-PCR were stained using LoadingSTAR (Dyne Bio, South

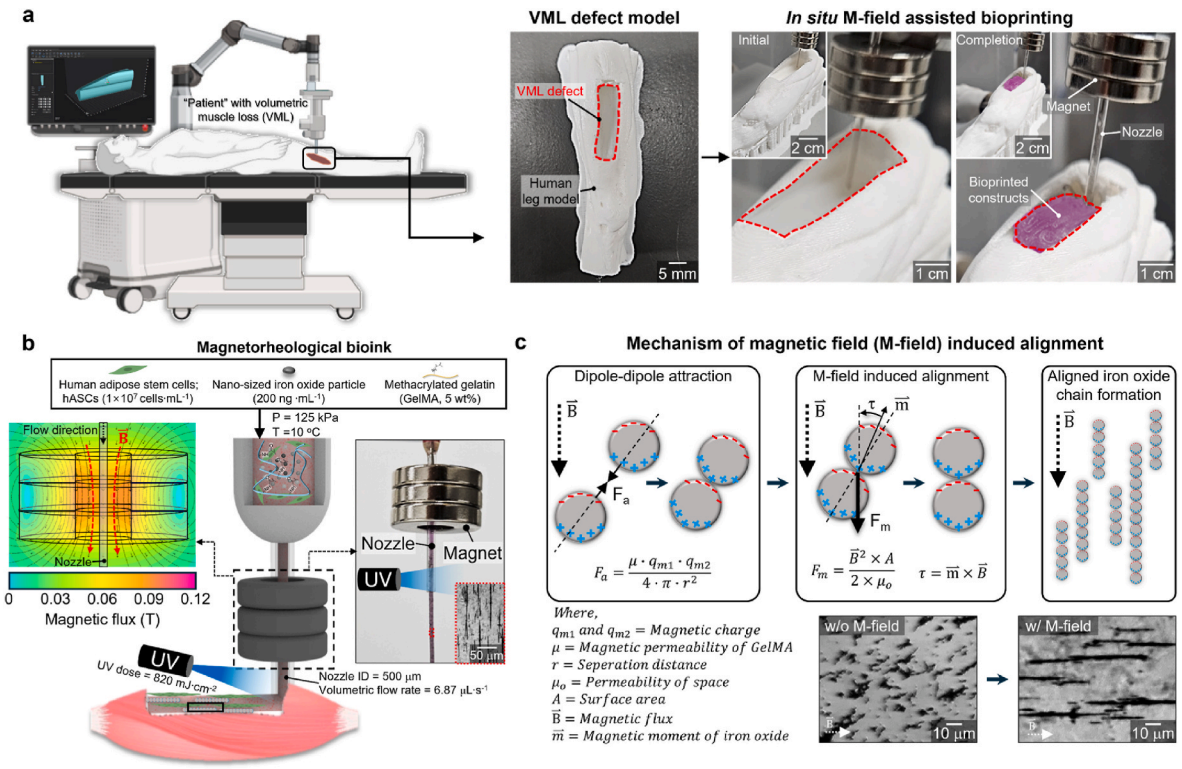

Fig. 1. Proof of concept for *in situ* M-field assisted bioprinting application. (**a**) Optical images of 3D printed VML defect model and *in situ* M-field-assisted bioprinted system onto the VML defect. (**b**) Schematic illustration of demonstrating the application of *in situ* M-field assisted bioprinting system and magnetic flux distribution around the nozzle. (**c**) Alignment mechanism and an optical image of the iron oxide particles under a magnetic field.

Korea) and separated on an agarose gel (1.2 %) *via* electrophoresis. Then, the images were captured using ChemiDoc XRS^{+} gel imaging system (Bio-Rad Laboratories, Hercules, Califonia, United States) with background removal function enabled. The captured images were adjusted using imageJ software as indicated in Supplementary Fig. S2 to enhance the visibility of the bands. The specific primer sequences utilized in this evaluation are detailed in Table S3.

2.7. Western blotting

Total proteins from cell lysates and tissue homogenates in bioconstructs were harvested by RIPA Buffer (Thermo Fisher Scientific) containing Protease/Phosphatase Inhibitor Cocktail (Thermo Fisher Scientific). The isolated total protein concentration was quantified using a BCA protein assay and equal amounts of protein were loaded onto SDS-PAGE gels, separated by electrophoresis, and transferred onto PVDF membranes. The membranes were blocked with 3 % BSA in TBS-T (Tris-buffered saline with 0.1 % Tween-20) for 1 h at room temperature and incubated overnight at 4 °C with primary antibodies [mouse anti-MF20 (dilution ratio 1:200 in PBS; Developmental Studies Hybridoma Bank, USA), rabbit anti-α-actinin (dilution ratio 1:2000 in PBS; PA5-27863; Invitrogen), and mouse anti-β-actin (dilution ratio 1:2000 in PBS; PA1-183; Invitrogen] specific to the target proteins. After washing with TBS-T, the membranes were incubated with HRP-conjugated secondary antibodies for 1 h at room temperature. Protein bands were visualized using an enhanced chemiluminescence substrate and imaged using a gel documentation system. Band intensities were quantified using ImageJ software and normalized to GAPDH as a loading control.

2.8. VML defect model

To investigate how bioprinted muscle constructs perform *in vivo*, we conducted surgeries on 10-week-old male C57BL/6 mice from DooYeol Biotech, Inc., Korea. These procedures were carried out following the approved protocol (GIST-2023-017) of the Animal Care and Use Committee of the Gwangju Institute of Science and Technology (GIST) in South Korea. Before surgery, mice were anesthetized with 3 % isoflurane. Then an incision on the skin of the lower left leg was made and separated the muscle from the fascia. We removed certain muscles to prevent compensatory hypertrophy and took out around 40 % of the TA muscles. Additionally, the weight of the TA muscles was calculated using the following equation, y (g) = 0.0017 × body weight (g) × 0.0716. Then, the bioconstructs of G, GIO, and GIOM. SHAM and non-treated (Defect) groups were used as controls. The bioconstructs were placed directly onto the defect sites without the use of bioadhesives. After 4 weeks of implantation, every group comprising a total of 15 mice (n = 3/group) was euthanized to evaluate *in vivo* muscle tissue restoration. The TA muscle from each lower limb was harvested and weighed.

Following the implantation of the fabricated bioconstructs, muscle functionality in the mice was evaluated using grip strength and hanging tests at four-time points (1, 2, 3, and 4 weeks). For the hanging test, each mouse was placed on a horizontal metallic rod, allowing the animal to grip the rod with its hindlimbs. The latency to fall, defined as the time until the mouse released its grip and fall, was recorded for a maximum of 5 min. Each trial consisted of five attempts, and the average latency was calculated to assess muscle endurance and strength. Regarding the grip strength test, a grip strength meter (BIO-G53; BIOSEB, USA) with a pull-grid assembly was used. Mice were allowed to grip the grid while being gently pulled horizontally by the tail until their grip was released. The device measured the maximum force exerted by the mouse before letting go. Each trial consisted of three measurements per mouse, with 5-min intervals between measurements to minimize fatigue. This process was repeated for each mouse across three independent trials, and the results were averaged to ensure accuracy and reproducibility.

To histologically assess muscle tissue regeneration, the collected TA muscles were fixed with 10 % neutral buffered formalin (NBF),

embedded in paraffin, followed by sectioning into thin sections (5 μm). These sections underwent deparaffinization and were then stained using H&E and MT staining. Quantitative analysis involving muscle fiber diameter (n = 25), the count of myofibers with peripherally positioned nuclei (n = 3), and the measurement of fibrotic area (n = 3) was conducted utilizing ImageJ software.

For further evaluation of VML muscle regeneration, the deparaffinized samples were subjected to incubation with primary antibodies including anti-mouse or anti-rabbit MHC (5 μg mL^{-1} in PBS; Santa Cruz Biotechnology, USA), human leukocyte antigen (HLA, human species reactivity) (5 μg mL^{-1} in PBS; Abcam, UK), human mitochondrial ribosomal protein L11 (MRPL11, species reactivity: human) (5 μg mL^{-1} in DPBS; Abcam, UK) and CD31 (5 μg mL^{-1} in PBS; Invitrogen). Following rinsing with PBS, the stained sections were counterstained with DAPI and incubated with Alexa Fluor 488-conjugated anti-rabbit (1:50 in PBS; Invitrogen) or Alexa Fluor 594-conjugated anti-mouse (1:50 in PBS; Invitrogen) secondary antibodies for 1 h. Observation of the stained tissues was performed using a Zeiss confocal microscope. Quantification of the MHC positive area, HLA, and MRPL11 positive cell frequency, and vessel area was carried out using ImageJ software.

2.9. Statistical analysis

Statistical analyses were carried out using the SPSS software (SPSS, Inc., USA). Student's t-test was utilized for comparing two groups, while single-factor analysis of variance (ANOVA) followed by Tukey's honest significant difference (HSD) post-hoc test was employed for comparing three or more groups. Statistical significance was considered at $^{*}p < 0.05$, $^{**}p < 0.01$, and $^{***}p < 0.001$.

3. Results and discussion

Despite recent advancements in various *in situ* bioprinting systems, the simple deposition of bioconstructs can lead to inadequate tissue regeneration and integration with the host tissue [33]. To address these challenges, stimulus-assisted bioprinting has emerged as a promising approach for modulating the cellular functions of implanted bioconstructs.

To address this issue, we developed a modified bioprinting technique employing an *in situ* M-field to align magnetically activated particles within a bioink during extrusion. As depicted in the images of Fig. 1a, we fabricated a model of a 'patient' with a VML defect in the thigh muscles. The VML defect region was then filled using our newly proposed *in situ* M-field-assisted bioprinting method, demonstrating that the magnetically activated bioink was stably deposited onto the defective region.

To observe the M-field distribution using the ring magnets, a simulated result showing the cross-sectional M-field distribution for the three ring-shaped magnets (maximum magnetic flux = 0.09 mT) confirmed the formation of a parallel distribution of the applied M-field, aligned with the flow direction of the bioink, shown in the optical image (Fig. 1b). Furthermore, to select the proper concentration of iron oxide nanoparticles laden in GelMa bioink (5 wt%) and the crosslinking condition using UV dose we simply tested the iron oxide alignment and cell-viability of hASCs of the bioink for various concentrations of the particles and mechanical property for various UV doses. To determine cell-viability and iron oxide alignment within the bioprinted constructs using the M-field (three ring magnets), various concentrations (50–500 ng mL^{-1}) of iron oxide nanoparticles (0.23 ± 0.06 μm) were loaded onto 5 wt% GelMA solutions containing hASCs (1×10^7 cells•mL^{-1}) under the UV dose (820 mJ cm^{-2}) and the printing conditions shown in Fig. 1b. Supplementary Figs. S3a and S3b show the alignment of iron oxide increased when the concentration increased from 50 to 200 ng mL^{-1}, but remained constant at 500 ng mL^{-1}. Since the magnetic field induced alignment of the iron oxide particles, it can be assumed that the ink's magnetism was weaker at lower concentrations (50 and 100 ng mL^{-1}), with a more significant impact on magnetism at higher concentrations where particle alignment was greater. Additionally, the cell viability on 1 and 7 d remained relatively high (~90 %) from 50 to 200 ng mL^{-1}, but significantly decreased at 500 ng mL^{-1} (Supplementary Figs. S3c and S3d). These results are similar to previous research, which indicates that the concentrations of iron oxide-based particles around 200 ng mL^{-1} are generally considered safe, while at higher concentrations, cellular activities including cell viability, growth, and proliferation were markedly reduced (Supplementary Table S1).

Supplementary Fig. S4a showed stress-strain curves of the bioconstructs (iron oxide particle concentration = 200 ng mL^{-1}) fabricated using various UV crosslinking conditions (UV dose = 125–1650 mJ cm^{-2}). The tensile modulus gradually increased with UV dose (Supplementary Fig. S4b). As a result, similar tensile moduli between bioconstructs fabricated using UV doses over the 820 mJ cm^{-2} implied that the methacrylate functional groups have been fully crosslinked over the dose. To evaluate the effects of UV radiation on cellular activities, the bioconstructs fabricated using various UV doses were stained using live/dead after 1 d, and DAPI/phalloidin after 3 d (Supplementary Fig. S4c). As expected, both cell viability and the F-actin area showed a considerable decline at high UV radiation (>1500 mJ cm^{-2}), indicating cellular damage (Supplementary Figs. S4c and S4d). Whereas, at lower UV irradiation (150–450 mJ cm^{-2}), although high cell viability (~90 %) was observed, the F-actin area was considerably lower, likely due to rapid degradation of the structure (Supplementary Fig. S4e). Based on the results, we fixed the iron oxide concentration at 200 ng mL^{-1} in the bioink and the UV crosslinking condition at 820 mJ cm^{-2}.

To evaluate the printability of the selected parameters, we conducted a filament collapse test using pillars with varying gap widths (1–6 mm) under three bioprinting conditions: G (conventional extrusion with *in situ* UV crosslinking), GIO (extrusion of magnetorheological bioink), and GIOM (extrusion of magnetorheological bioink with an external magnetic field), as illustrated in Supplementary Fig. S5a. The test revealed no collapse or deformation of the extruded struts in any group, demonstrating the excellent printability of the developed system. Additionally, to further validate the 3D printing capabilities under these conditions, the system successfully modeled and printed the letters "SKKU," highlighting its precise and robust performance (Supplementary Figs. S5b and S5c).

The schematic in Fig. 1c illustrates the physical phenomenon affecting magnetizable particles under an M-field, leading to the uniaxial alignment of chained iron oxide particles. This alignment occurs due to the force (F_a) of dipole-dipole interaction and the subsequent magnetically activated torque (τ), where $\tau = \vec{m} \times \vec{B}$, with ' $\vec{m}$' representing the magnetic moment of the chained iron oxide particles and ' $\vec{B}$' the magnetic flux.

For spherical particles under the M-field, the magnetic moment can be calculated as $\vec{m} = 12.6\mu_0\mu_c r^3[(\mu_i-\mu_c)/(\mu_i+2\mu_c)]B_o$, where μ_0 is the permeability of vacuum, μ_c is the relative permeability of the continuous phase (in our case, GelMA hydrogel), μ_i is the relative permeability of the magnetizable particle (e.g., iron oxide), 'r' is the radius of the spherical particle, and B_0 is the magnetic flux [34–36].

Through this physical mechanism, the magnetizable particles can be chained and aligned in the direction of the M-field, as shown in the optical image in Fig. 1c. After the fabrication of the aligned chains of particles in the flow direction, UV light was used to crosslink the GelMA-based bioink simultaneously, maintaining the structural integrity post-extrusion. Finally, the aligned chain particles within the crosslinked GelMA structure served as spatial topographical cues, significantly influencing the alignment and myogenic differentiation of the embedded hASCs. This is crucial for developing biomimetic muscle structures and enhancing the functional properties of the regenerated muscle tissues.

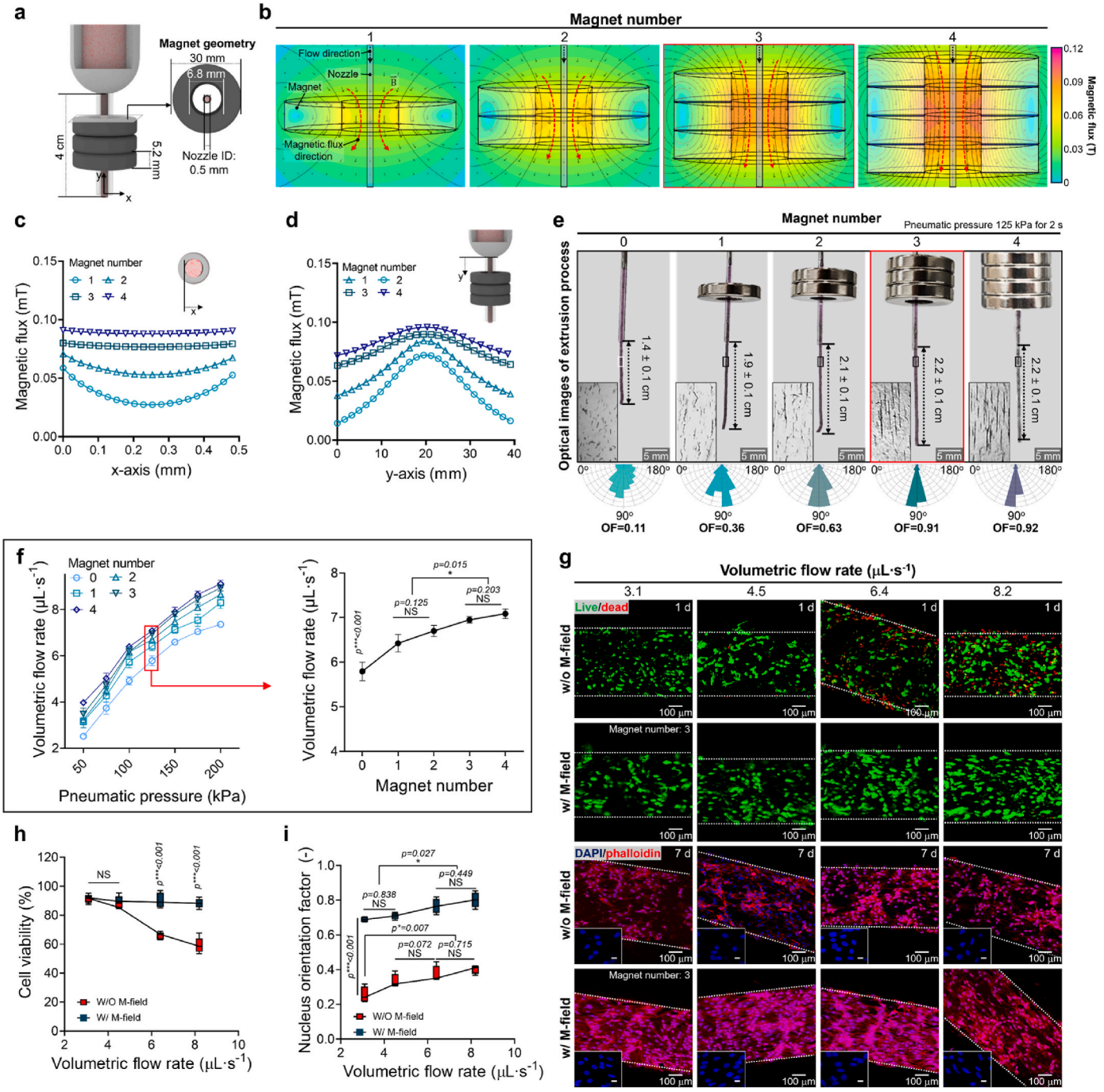

Fig. 2. Evaluation of M-field intensity on flowability of magnetorheological bioink. (**a**) A schematic representation of *in situ* M-field assisted bioprinting system. (**b**) Magnetic simulation distribution around the nozzle with various magnet numbers and calculated magnetic flux along the (**c**) x-axis and (**d**) y-axis for the magnet numbers. (**e**) Optical images of extruded bioink struts for various magnet numbers and (**f**) measured volumetric flow rates of bioink for various pneumatic pressures (50–200 kPa) and magnet numbers (n = 5). (**g**) Live (green)/dead (red) images after 3 d, and DAPI (blue)/phalloidin (red) images after 7 d of hASCs cultured in bioconstructs fabricated w/and w/o *in situ* M-field and subjected to various volumetric flow rates (3.1–8.2 μL s^{-1}). Quantification of (**h**) cell viability (n = 5) and (**i**) nucleus orientation factors of samples (n = 5).

3.1. Analysis of magnetic field distribution and its effect on the flowability of the bioink within a nozzle

To determine the M-field distribution generated by the ring magnets, we positioned a varying number of magnets around the nozzle, maintaining fixed geometry for each magnet (inside radius = 6.8 mm, outside radius = 10 mm, thickness = 5.2 mm) (Fig. 2a). The distribution of magnetic flux around the printing nozzle was calculated using the finite element method magnetics (FEMM) software. As expected, the M-field vectors were aligned parallel to the glass nozzle direction (Fig. 2b), facilitating the uniaxial alignment of the iron oxide particles within the bioink.

Furthermore, to observe the effect of the number of magnets on the M-field distribution, simulations were conducted using one-to four-ring magnets. The results shown in Fig. 2b reveal a homogeneous M-field distribution with three-ring magnets. To quantitatively assess the M-field distribution, Fig. 2c and d depict the magnetic flux profiles relative to the midplane of the magnet, perpendicular (x-axis), and parallel (y-

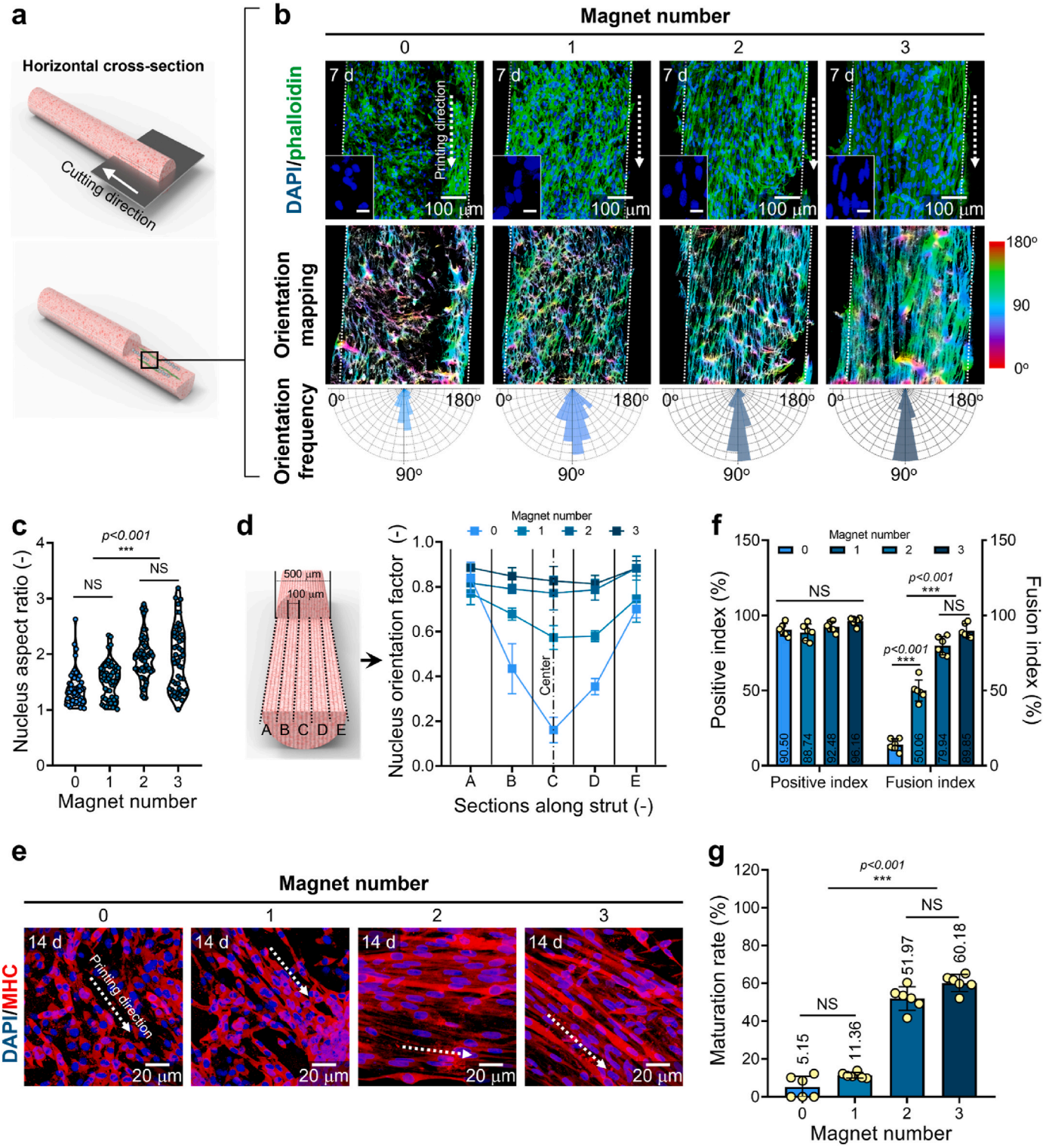

Fig. 3. Characterization of cellular morphologies and myogenic activities with various M-field intensity. (**a**) Schematic diagram of horizontal cross-section images and (**b**) DAPI/phalloidin (green) images, orientation mapping, and measured orientation frequencies in hASCs viewed from horizontal cross-section cultured for 7 d. Quantification of (**c**) aspect ratio (n = 25) and (**d**) orientation factors of nuclei for various magnet numbers (n = 5). (**e**) DAPI/MHC (red) images after 14 d of hASCs bioprinted with various magnet numbers. Measured (**f**) positive and fusion index (n = 6), and (**g**) maturation rate (n = 6) of hASCs using DAPI/MHC images.

axis) to the nozzle length. The graphs demonstrate that increasing the number of magnets significantly enhances the intensity and homogeneity of the magnetic flux in both directions. In particular, a homogeneous magnetic flux along the x-axis is important for achieving a uniform distribution of chain-like particles perpendicular to the bioprinted struts. Based on the simulation results, three magnets appear to be sufficient to achieve a homogeneous alignment of magnetic particles within the bioink.

Exposing a magnetically responsive hydrogel to an M-field can alter its rheological properties, including viscosity, by reorganizing magnetic

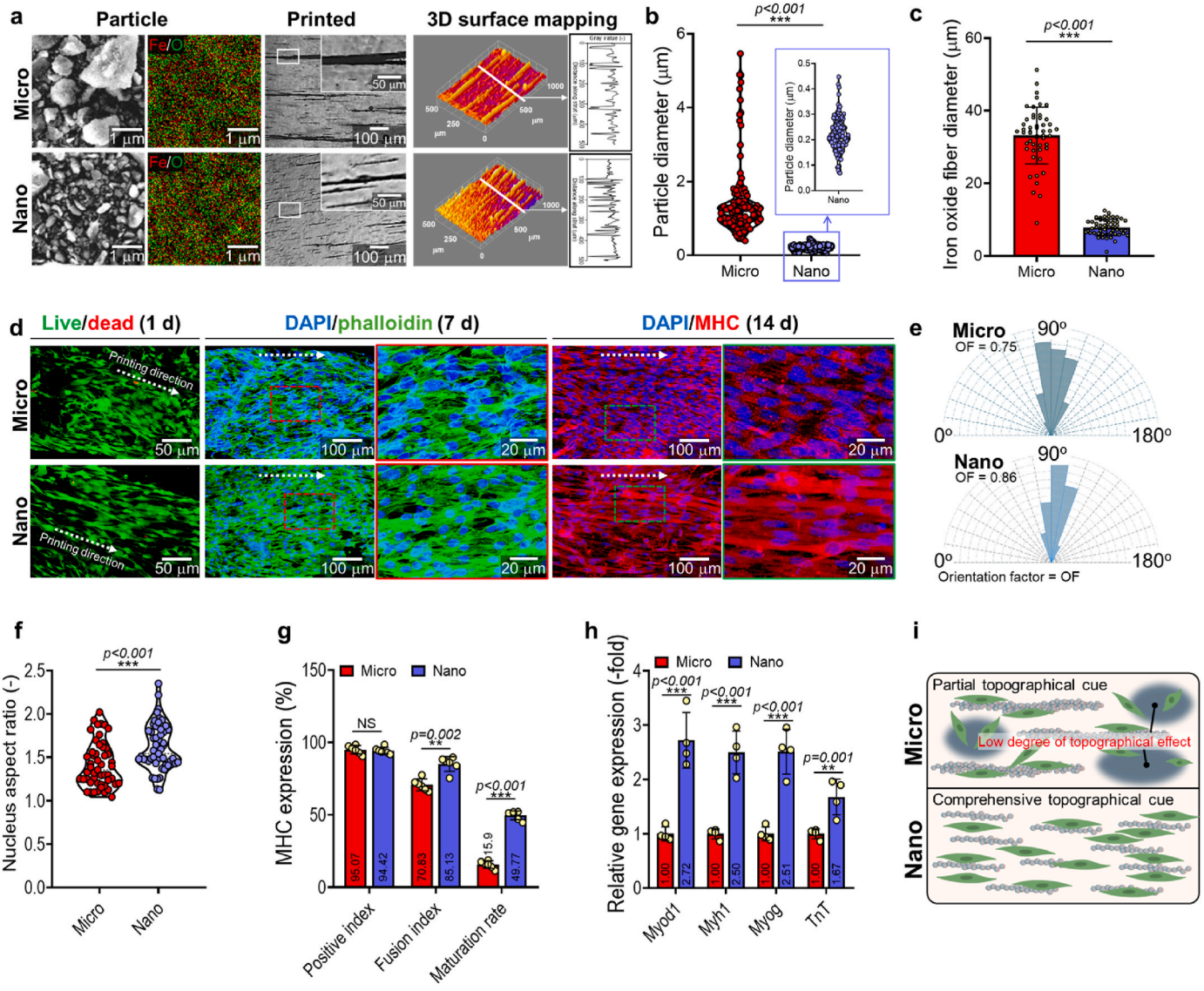

Fig. 4. Characterization and biological effects of magnetorheological bioink incorporated with nano- and micro-sized iron oxide particles. (**a**) SEM images and EDS mapping of nano- and micro-sized iron oxide particles, optical microscopy images, and 3D surface mapping of printed GelMA/iron oxide bioink using *in situ* M-field assisted bioprinting. (**b**) Measured particle diameter (n = 25) and (**c**) iron oxide fiber diameter (n = 25). (**d**) Live/dead images after 1 d, DAPI/phalloidin images after 7 d, and DAPI/MHC images after 14 d of hASCs fabricated with micro- or nano-sized iron oxide particles. The measured distribution of (**e**) nucleus orientation and (**f**) aspect ratios (n = 25) from DAPI images. (**g**) Quantified MHC positive, fusion, and maturation rate from DAPI/MHC images (n = 6). (**h**) Relative myogenesis-related gene expressions including Myod1, Myh1, Myog, and TnT (n = 4). (**i**) Schematics showing the different status of cell alignment and chained particles consisting of nano- and microparticles.

particles within the hydrogel matrix. When a magnetorheological bioink is subjected to an M-field, the magnetized particles tend to align parallel to the M-field lines, which significantly influences the rheological properties of the fluid by aligning the chains of the magnetic particles. Empirically, an externally applied M-field can reduce the wall shear stress of the bioink within the nozzle, thereby improving its flowability.

To observe this effect, we measured the length of the extruded strut after 2 s of extrusion at a fixed pneumatic pressure (125 kPa) (Fig. 2e). The results showed that increasing the number of magnets (and thus the magnetic flux) led to longer extruded bioink lengths, indicating that the flow resistance in the nozzle was significantly reduced owing to the alignment of magnetic particles. The results showed that increasing the number of magnets (and thus the magnetic flux) led to longer extruded bioink lengths, indicating that the flow resistance in the nozzle was significantly reduced owing to the alignment of magnetic particles. The alignment generates a magnetic force parallel to the flow direction, which actively assists the bioink's movement through the nozzle. This assisting force reduces resistance, resulting in improved the bioink flows and enhancing extrusion length as the magnetic flux increases. Additionally, the volumetric flow rates measured under various pneumatic pressures (50–200 kPa) and different numbers of magnets (0–3) indicated higher flow rates with the application of both pneumatic pressure and M-fields (Fig. 2f). These data suggest that external M-fields, aligned with the bioink flow, can significantly lower the wall shear stress in the nozzle, ensuring safer conditions for cells within the bioink than for those not treated with ring magnet.

To evaluate the accuracy of the hypothesis, we extruded iron oxide-incorporated bioinks with (w/) and without (w/o) *in situ* M-field at various volumetric flow rates (3.1–8.2 μL s^{-1}). The cells were stained with live/dead after 3 d and DAPI/phalloidin (Fig. 2g). As expected, cell viability decreased with higher volumetric flow rates in bioinks not exposed to the M-field, indicating that increased flow rates induced cell damage due to high wall shear stress (Fig. 2h). In contrast, bioinks exposed to the M-field showed relatively high cell viability (~90 %),

suggesting a reduction in wall shear stress. Additionally, the cellular alignment shown in Fig. 2i indicates a gradual increase in orientation with the bioink's volumetric flow rate. Notably, bioinks processed using *in situ* M-field-assisted bioprinting resulted in significantly higher anisotropic organization of cells.

The bioink's flowability was evaluated by comparing two magnet setups: a ring-shaped magnet and a box-shaped magnet, which provide parallel and perpendicular magnetic flux relative to the bioink flow direction as illustrated by the FEMM simulation results, shown in Supplementary Fig. S6a. The optical image in Supplementary Fig. S6b reveals a shorter extruded length with the perpendicular magnet setup, indicating a disturbance in the bioink's flowability. Additionally, volumetric flow rate measurements under various pressures showed a significant reduction with the perpendicular magnet setup (Supplementary Fig. S6c), further demonstrating its negative impact on flowability. These results are further complemented by the rheological evaluation where the vector of the M-field is applied perpendicular to the rotation of the plate (Supplementary Fig. S7a). As a result, the storage modulus (G′) and complex viscosity (η*) of the magnetorheological bioink exhibited a significant increase for the temperature sweep when subjected to a magnetic field of 0.09 mT (Supplementary Figs. S7b–d). This increase can be clearly attributed to the formation of perpendicular iron oxide chains, which impede the rotational flow of the bioink.

3.2. Cell alignment and myogenic activities for the cell-constructs bioprinted with various magnetic fields

To assess biological activities, specifically cell alignment due to topographical cues induced by the aligned particle chains, and myogenic activity, we performed staining on the horizontal cross-section of cell-laden bioconstructs composed of 5 wt% GelMA, iron oxide (200 ng mL^{-1}), and hASCs (1×10^7 cells•mL^{-1}) fabricated with varying numbers of ring magnets (0–3) (Fig. 3a). We performed DAPI and phalloidin staining, orientation mapping (90° was the printing direction), and orientation frequency analysis of hASCs after 7 d to evaluate cell alignment (Fig. 3b).

Quantitative analysis of DAPI/phalloidin images revealed a gradual increase in the cell nucleus aspect ratio, with 1.11-fold (one magnet), 1.39-fold (two magnets), and 1.38-fold (three magnets) increases compared to the no-magnet process (Fig. 3c). Furthermore, we evaluated the alignment of nuclei along the struts using the orientation factor equation, orientation factor = (90° – φ)/90°, where φ is the full width at half maximum (FWHM) of the orientation angle distribution.

Fig. 3d shows the distribution of the nucleus orientation factors across five regions perpendicular to the printing direction. For the no-magnet process, cell alignment was predominantly achieved near the wall region, with poor orientation in the central region. However, with the application of magnets, the difference in nucleus orientation between the center and wall regions gradually decreased as the number of magnets increased. Notably, with the three-ring magnets, the orientation in the central region was almost identical to that in the wall region, exhibiting a high orientation factor (approximately 0.9). These results confirmed that bioconstructs processed with M-field assistance exhibited significant and homogeneous cellular alignment, independent of the printed strut region, suggesting more homogeneous myogenesis compared to conventionally bioprinted cell constructs.

To evaluate the myogenic activities of the cells fabricated using the magnet-assisted process, we quantified the myosin heavy chain (MHC) staining images by calculating the positive index (percentage of MHC-positive nuclei), fusion index (percentage of myotubes with two or more nuclei), and maturation rate (percentage of myotubes with five or more nuclei) (Fig. 3e and Supplementary Fig. S8). While the cells exhibited a high MHC-positive index (approximately 90 %) across all groups, the MHC fusion index and maturation rate were accelerated in cells stimulated with a higher number of M-field (Fig. 3f and g). These results confirm that the application of the three-ring magnet provides a homogeneous magnetic flux around the printing nozzle, promoting significant cellular alignment and enhancing the myogenic activity of the cells.

3.3. Effects of nano- and micro-iron oxide particles laden in the bioink on cellular activities

Fig. 4a presents scanning electron microscopy (SEM) images and energy dispersive X-ray spectroscopy (EDS) elemental mapping of micro- and nano-sized iron oxide particles, along with optical images showing chained particles within the GelMA matrix printed using M-field-assisted bioprinting (with three-ring magnets). The 3D surface mapping images illustrate the diameters of the particle chains in each fabricated structure. Assessment of the chemical components [iron (Fe, red) and oxygen (O, green)] on the iron oxide particles showed the presence of both iron and oxygen, confirming the composition of iron oxide. The average diameters of the particles were approximately 0.22 μm (nano-sized) and 1.44 μm (micro-sized) (Fig. 4b). Exposure to the *in situ* M-field resulted in the aggregation of micro-sized iron oxide particles into larger fibers compared to the aggregation of nano-sized particles (Fig. 4c).

Generally, smaller topographical cues, particularly at the nanoscale or submicron scale, provide a more conducive environment for myogenic activities by enhancing cell-matrix interactions, alignment, mechanical signaling, and gene expression owing to a higher surface area-to-volume ratio. Specifically, the myogenic potential of hASCs is highly dependent on micro- and nanoscale topographical cues that affect the dynamic rearrangement of cytoskeletal structures, thereby altering cellular behavior.

To investigate the effect of magnetic chains comprising micro- and nano-sized particles, we incorporated these particles into the hASC-laden GelMA bioink for *in situ* M-field-assisted bioprinting. Cell proliferation rates, evaluated using the MTT assay, indicated that cells proliferated throughout the culture period in both the micro- and nano-sized iron oxide particle-incorporated bioconstructs (Supplementary Fig. S9a). Fig. 4d shows live/dead, DAPI/phalloidin, and DAPI/MHC images of bioconstructs containing micro- or nano-sized iron oxide particles after 1, 7, and 14 d of culture, respectively. The cell viability, as shown in Supplementary Fig. S9b, was relatively high (>90 %), indicating that the incorporation of both types of particles did not adversely affect the cultured cells.

Cellular alignment analysis revealed that bioconstructs containing nano-sized particles exhibited a 1.14-fold higher orientation factor (Fig. 4e) and 1.14-fold higher aspect ratio (Fig. 4f) than those with micro-sized particles. The myogenic activity was quantitatively assessed based on MHC positivity, MHC fusion, and maturation (Fig. 4g). Constructs with nano-sized aligned particles exhibited significantly higher MHC fusion and maturation. Furthermore, the expression levels of myogenic genes [myogenic differentiation 1 (Myod1), myosin heavy chain 1 (Myh1), myogenin (Myog), and troponin T (TnT)] were significantly higher in the constructs with nano-sized particles than in those with micro-sized particles (Fig. 4h).

These results align with those of previous studies, showing that smaller topographical cues induce more efficient cell alignment and enhance myogenic activity. This phenomenon can be further explained by the coarse topography formed by the larger fibers, which may create irregularities within the GelMA matrix, as depicted in Fig. 4i. Such irregularities can disrupt the continuous and homogeneous cell distribution during bioprinting. In contrast, nano-sized particles tend to form finer fibers, resulting in a more uniform and smaller topography that facilitates better cell alignment along the printed structures. These variations in topography influence cellular behavior and myogenic activities within cell constructs, thereby impacting the overall functionality and integration of bioprinted tissues. Therefore, we posit that aligning nano-sized iron oxide particles through *in situ* M-field-assisted bioprinting can provide the necessary topographical cues to achieve

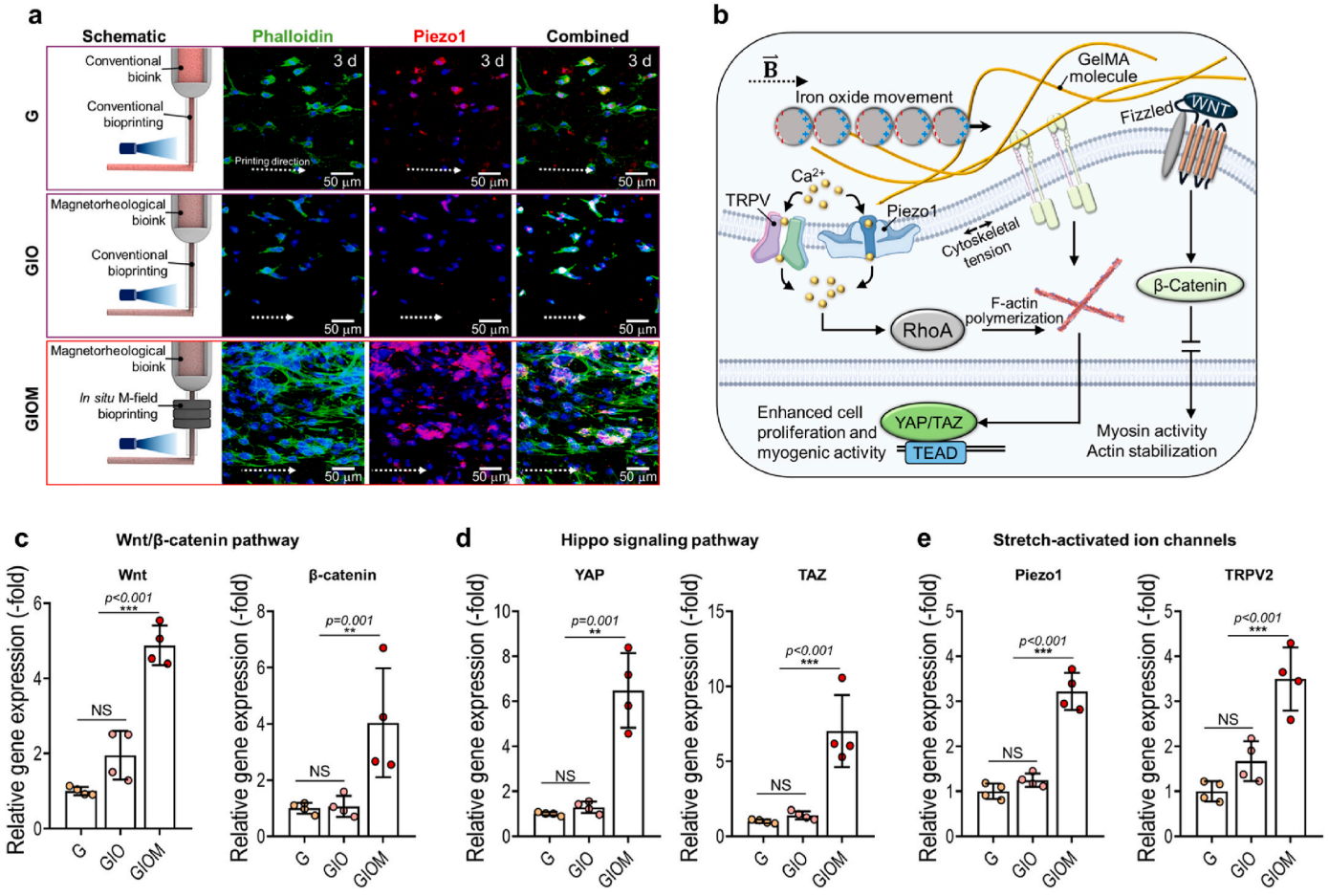

Fig. 5. Effects of *in situ* M-Field assisted bioprinting on mechanotransduction signaling pathways. (**a**) A schematic diagram illustrating fabrication process and DAPI/phalloidin/piezo1 (red) images of cells cultured in G, GIO, and GIOM. (**b**) Schematics demonstrating mechanotransduction-related cellular pathways stimulated *via* movement of iron oxide particles through *in situ* M-field. Relative expressions of genes in (**c**) Wnt/β-catenin signaling pathway (Wnt and β-catenin) (n = 4), (**d**) hippo signaling pathway (YAP and TAZ) (n = 4), and (**e**) stretch-activated ion channels (Piezo1 and TRPV2) (n = 4) of hASCs after 3 d of culture.

optimal cellular alignment.

3.4. Mechanotransduction effects of a M-field assisted bioprinting process

The presence of an M-field in the bioprinting process can evoke the polarization of iron oxide particles, inducing a magnetic attraction force. In regard to *in situ* M-field-assisted bioprinting can stimulate mechanotransduction signaling pathways in cells and induce favorable cellular responses. To evaluate this phenomenon, 'G' (conventionally bioprinted hASCs-laden GelMA bioconstruct), 'GIO' (conventionally bioprinted iron oxide/hASCs-laden GelMA), and 'GIOM' (*in situ* M-field assisted bioprinted hASCs/iron oxide-laden GelMA bioconstruct) are prepared (Fig. 5a).

Mechanotransduction pathways are pivotal in the cellular response to mechanical stimuli and influence diverse biological functions (Fig. 5b). Among these pathways, the hippo signaling pathway, Wnt/β-catenin pathway, and ion channels can play important roles in regulating cellular processes such as cell growth, differentiation, signaling, and homeostasis. The Hippo pathway is sensitive to mechanical signals and governs cell behavior by regulating proliferation, differentiation, and tissue growth [37–39]. Alterations in cell shape and cytoskeletal tension induced by mechanical cues modulate Hippo pathway activity, thereby impacting gene expression and cell destiny. Similarly, the Wnt/β-catenin pathway integrates mechanical and biochemical signals to control cell fate, growth, and differentiation during development and tissue maintenance [40]. Mechanosensitive ion channels, such as stretch-activated channels, contribute to cellular mechanotransduction by converting mechanical forces into electrochemical signals, thereby influencing gene expression, cell motility, and differentiation [41]. Through an intricate interplay and adjustment, these mechanotransduction pathways collectively steer cellular responses to mechanical stimuli and play key roles in tissue development, maintenance, and pathological processes [42]. Therefore, we predicted that cells that were mechanically stimulated using *in situ* M-field bioprinting method could further initiate the aforementioned cell signaling pathways, leading to favorable cellular responses.

To evaluate the accuracy of this hypothesis, cells cultured on the G, GIO, and GIOM bioconstructs were stained using DAPI/phalloidin/piezo1 after 3 d of culture, as shown in Fig. 5a. After extrusion of the magnetically active bioink through an *in situ* M-field, we noted that piezo1 was expressed significantly more than cells in the G and GIO bioconstructs. As piezo1 is a protein that functions as a mechanosensitive ion channel, meaning that it responds to mechanical stimuli such as tension, pressure, or stretch, we estimated that the developed system can effectively stimulate mechanotransduction activities in laden cells [43,44]. Furthermore, using quantitative real-time polymerase chain reaction (qRT-PCR) analysis, we quantified the expression levels of mechanotransduction-related genes, including components of the Wnt signaling pathway (Wnt and β-catenin) (Fig. 5c), hippo signaling pathway (YAP and TAZ) (Fig. 5d), and stretch-activated ion channels (Piezo1 and TRPV2) (Fig. 5e). We observed significant upregulation of these genes in the GIOM bioconstructs. These results suggest that mechanical stimulation induced by *in situ* M-field bioprinting plays an important role in augmenting cell proliferation and promoting the

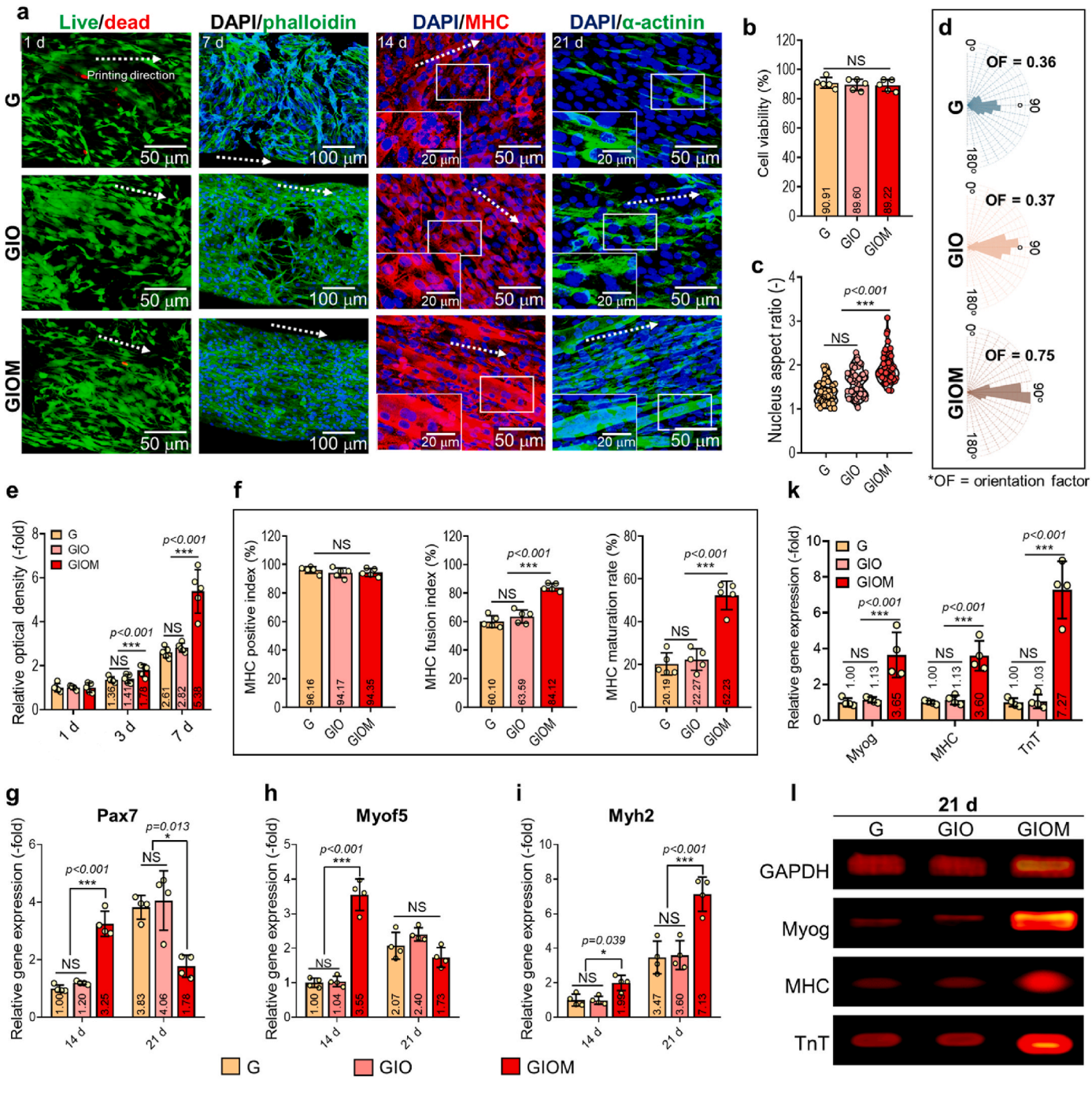

(caption on next page)

Fig. 6. ***In vitro*** **cellular activities of hASCs cultured in various GelMA constructs.** (**a**) Live/dead at 1 d, DAPI/phalloidin at 7 d, immunofluorescent images DAPI/MHC at 14 d, and DAPI/α-actinin (red) at 21 d of hASCs cultured in G, GIO, and GIOM bioconstructs. Measured (**b**) cell viability (n = 5), (**c**) nucleus aspect ratio (n = 5), (**d**) nucleus orientation of hASCs cultured in bioconstructs. (**e**) Cell proliferation determined using MTT assay (n = 5). (**f**) Quantification of MHC positive index, fusion index, and maturation rate (n = 5). Relative myogenesis-gene expressions of (g) Pax7, (h) Myof5, and (i) Myh2 (n = 4), and (j) agarose gel electrophoresis using qRT-PCR products of hASCs cultured in bioconstructs for 14 and 21 d. (**k**) Relative myogenesis-related gene expressions including Myog, MHC, and TnT (n = 4) and (**l**) agarose gel electrophoresis using qRT-PCR product after 21 d. (m) Western blotting of β-actin, MHC, and α-actinin from protiens extracted from hASCs cultured in bioconstructs for 21 d.

myogenic differentiation of bioprinted hASCs.

To further assess the impact of the mechanical stimulation provided by the proposed *in situ* M-field-assisted bioprinting, we compared it with the conventional method of bioprinting using the same bioink containing iron oxide nanoparticles (200 ng mL^{-1}), followed by post-printing M-field stimulation, as illustrated in Supplementary Fig. S10a.

Piezo1, a mechanosensitive ion channel important for various physiological processes, including myogenic activity, was used as a marker to evaluate mechanotransduction. We measured piezo1 expression using DAPI and phalloidin staining at 1 d post-fabrication (Supplementary Fig. S10b). The results indicated that piezo1 expression was notably higher in the *in situ* M-field-assisted bioprinted constructs than in the control group, which received continuous M-field stimulation after printing. This observation was corroborated by the significant upregulation of mechanotransduction-related genes, including Wnt, YAP, and Piezo1 in the *in situ* M-field-assisted group after 1 d (Supplementary Fig. S10c). Based on the results, the *in situ* M-field-assisted bioprinting process enhanced early mechanotransduction processes more effectively than post-printing M-field stimulation. This indicates the potential benefits of *in situ* bioprinting applications, which offer improved cellular responses and promising outcomes for muscle tissue development.

3.5. In vitro cellular response to in situ M-field stimulation

To assess various *in vitro* cellular responses of the G, GIO, and GIOM bioconstructs, we observed live/dead staining at 1 d, DAPI/phalloidin staining at 7 d, DAPI/MHC staining at 14 d, and DAPI/α-actinin staining at 21 d (Fig. 6a). Live/dead images indicated high cell viability (~90 %) for all three groups, demonstrating that the fabrication printing process was safe (Fig. 6b). DAPI/phalloidin images at 7 d were used to evaluate the cytoskeletal organization of hASCs within the bioconstructs, and the nuclei were quantitatively assessed for aspect ratio and orientation factor (Fig. 6c and d). The results showed that cells cultured in the GIOM bioconstruct exhibited a significantly greater aspect ratio, suggesting that these cells continuously received higher mechanical stimulation owing to topographical cues, which affected mechanotransduction pathways. The orientation factor, which can affect to the formation of structurally and functionally coherent muscle fibers, was also comparatively high (~0.75 for GIOM, ~0.36 and ~0.37 for G and GIO, respectively). Additionally, the MTT assay (Fig. 6e) indicated that the cells in all groups proliferated well over time, with cells proliferating at a considerably higher rate (2.1-fold and 1.9-fold at 7 d) compared to G and GIO, respectively, due to the early mechanotransduction effect.

The myogenic capabilities of cells in the bioconstructs were analyzed using immunofluorescence imaging of DAPI/MHC after 14 d and DAPI/α-actinin after 21 d (Fig. 6a). Quantitative analysis of the MHC-positive index, fusion index, and maturation rate revealed that cells in the GIOM group exhibited more efficient development of multinucleated myotubes than those in the G and GIO groups (Fig. 6f).

To further confirm the myogenic activities observed in the immunofluorescence images, we have assessed early myogenic markers paired box protein Pax-7 (Pax7) and myogenic factor 5 (Myof5) (associated with the determination state) and the late myogenic marker myosin heavy chain 2 (Myh2) (associated with the maturation state) were assessed at 14 and 21 d using qRT-PCR (Fig. 6g–i) and agarose gel electrophoresis (Fig. 6j and Supplementary Fig. S11). Notably, Pax7 and Myof5 exhibited relatively higher expression levels in the GIOM group compared to the G and GIO groups on 14 d but showed significant downregulation by 21 d, indicating a potential transition of cells from the determination phase to subsequent differentiation stages. In contrast, cells cultured in GIOM constructs demonstrate consistently higher expression of the maturation marker Myh2 at both time points, suggesting that the GIOM constructs provide a more conducive microenvironment for promoting myogenic differentiation and maturation. Furthermore, the expression levels of late-stage myogenesis-related genes (Myog, MHC, and TnT at 21 d) were quantitatively assessed at 21 d using qRT-PCR (Fig. 6k) and agarose gel electrophoresis (Fig. 6l and Supplementary Fig. S2). Interestingly, the incorporation of iron oxide particles (GIO) into the cell-loaded GelMA bioconstructs did not affect the expression of myogenesis-related genes, whereas exposure to the M-field significantly upregulated the expression of Myog, MHC, and TnT. These results demonstrate the potential of *in situ* M-field stimulation in the bioprinting process, which enhances various cellular activities and promotes strong myogenic activities. Furthermore, Western blot analysis shown in Fig. 6m showed stronger expressions for α-actinin and MHC proteins in the GIOM group, further supporting the enhanced maturation of myogenic cells in these constructs.

3.6. In vivo works

To further verify the *in vitro* findings, the bioconstructs (2 × 4 × 1 mm^2) were implanted directly into VML defects in mice after printing. As shown in Fig. 7a, approximately 40 % of the tibialis anterior (TA) muscles were removed. Subsequently, bioconstructs (G, GIO, and GIOM) were placed at the defect site for implantation (Fig. 7b). Age-matched (SHAM) and non-treated (Defect) mice were selected as positive and negative controls, respectively, to evaluate the regenerative efficacy of these constructs.

Four weeks after implantation, the TA muscles were harvested and subjected to histological evaluation using Hematoxylin and Eosin (H&E) and Masson's trichrome (MT) staining (Fig. 7c). From the images, analyzing parameters including myotube diameter, peripherally nucleated myofibers, and fibrotic areas were quantitatively assessed (Fig. 7d–f). Compared with mice that underwent defect treatment, those receiving G, GIO, and GIOM bioconstructs exhibited larger muscle fiber diameters, suggesting the facilitation of muscle regeneration through bioconstruct implantation. Notably, the GIOM group displayed the highest muscle diameter, indicating a 1.66-fold increase compared with the defect group. Furthermore, most myofibers in mice that received GIOM were peripherally nucleated, indicating near-complete muscle fiber regeneration. Conversely, substantial fibrotic areas were observed in the defect, G, and GIO groups, indicating significant fibrosis (Fig. 7f). Interestingly, the similarity in the fibrotic areas between the G and GIO groups suggests that the incorporation of iron oxide particles into the bioconstructs did not induce notable fibrosis.

Fig. 7g illustrates the TA muscle weights after 4 weeks of treatment, with values for SHAM, defect, G, GIO, and GIOM measured at 42.3, 25.2, 35.7, 36.7, and 39.2 g, respectively. These results indicated a considerable improvement in muscle weight following bioconstruct implantation after VML defects. Additionally, TA muscle functionality was evaluated through grip strength and latency-to-fall assessments at various time points during the 4 weeks implantation period (Fig. 7h and i). As shown, grip strength and latency to fall were significantly reduced in all groups immediately after VML defect induction (week 1). However, the mice that received implants demonstrated faster functional

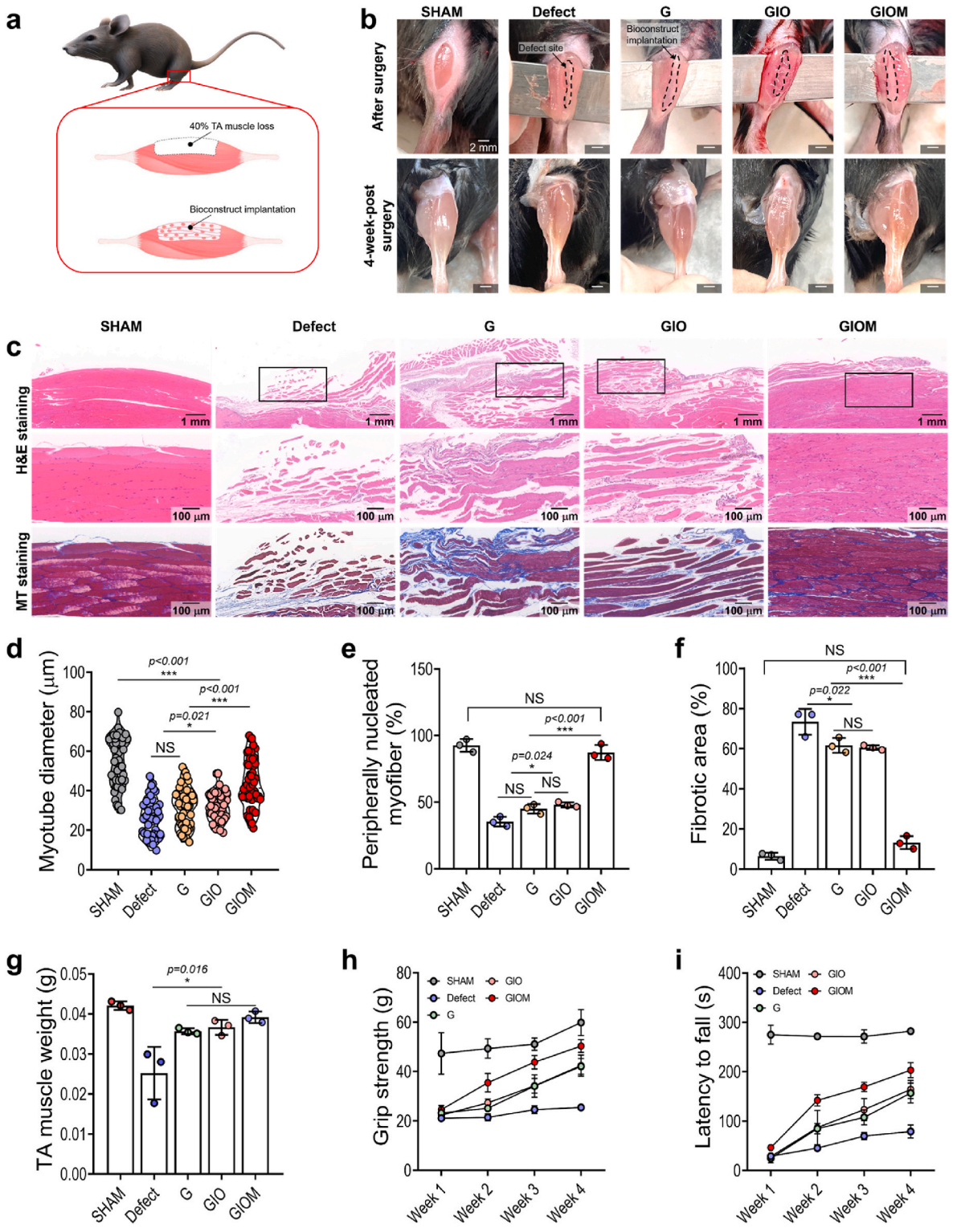

Fig. 7. ***In vivo*** **therapeutic effects of bioconstructs in mouse VML defect model.** (**a**) Schematic images of bioconstruct implantation procedure to VML defect, and (**b**) optical images directly after implantation and after 4 weeks of implantation. (**c**) H&E and MT histological staining of the implantation site and measured (**d**) myotube diameter (n = 25, animal number = 3), (**e**) peripherally nucleated myofiber (n = 3, animal number = 3), and (**f**) fibrotic area (n = 3, animal number = 3). Measured (**g**) TA muscle weight after 4 weeks of implantation (n = 3, animal number = 3), (**h**) grip strength (1, 2, 3, 4 weeks after implantation) (n = 3), and (**i**) latency to fall (1, 2, 3, 4 weeks after implantation) (n = 3, animal number = 3).

recovery than those with the defect alone, highlighting the beneficial effects of the bioconstructs on muscle regeneration. Notably, by the end of the 4 weeks implantation period, the GIOM group exhibited increased grip strength and prolonged latency to fall, suggesting an active role of GIOM in restoring lost functionality in VML defects.

To identify the cellular types and origins within the TA muscle, we used immunochemical staining with markers for the MHC, human leukocyte antigen (HLA), human mitochondrial ribosomal protein L11

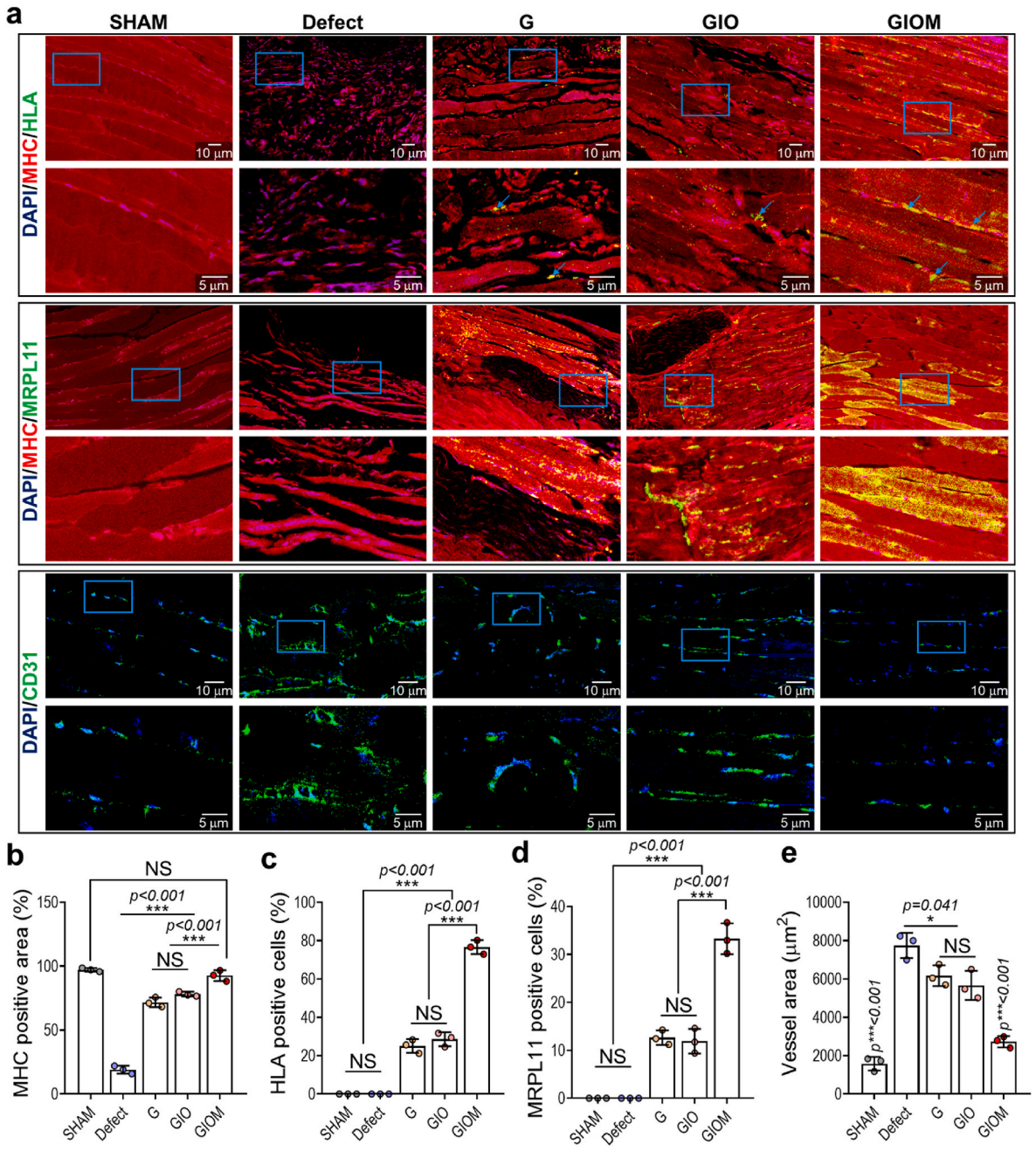

Fig. 8. Immunochemical staining analysis of muscle regeneration, and vascularization. (**a**) Immunochemical staining images of DAPI/MHC/HLA (green), DAPI/MHC/MRPL11 (green) and DAPI/CD31 (green) of the muscle harvested from the mice 4 weeks after implantation. Quantification of (**b**) MHC positive area, (**c**) HLA positive cells (n = 3, animal number = 3), (**c**) MRPL11 positive cells (n = 3, animal number = 3), and (**3**) vessel area (n = 3, animal number = 3).

(MRPL11) and CD31 to specifically label endothelial cells (Fig. 8a and Supplementary Fig. S12a). Assessment of the MHC-positive area (Fig. 8b) revealed a notably higher expression in the GIOM group than in the defect, G, and GIO groups, approaching levels similar to those in the SHAM group. Remarkably, both HLA and MRPL11, which has human reactivity, was absent in the SHAM and defect groups but was positively expressed in the implant groups (G, GIO, and GIOM), suggesting the successful integration of implanted hASCs with the host tissue (Fig. 8c and d). Particularly, a substantial proportion of cells within the TA muscle of the GIOM group exhibited HLA expression, implying that mechanical stimulation facilitated the integration of hASCs with the host tissue.

After a VML defect, the host initiates muscle recovery through the rapid ingrowth of intricate vascular networks. However, as the regeneration process unfolds, these vascular structures undergo remodeling, transitioning into microvessels dispersed among the mature muscle fibers [6,45]. Quantification of the vessel area based on CD31 expression, as depicted in Fig. 8e, underscores the significant formation of vascular areas in the VML group resembling the initial stages of muscle regeneration. Importantly, our observations revealed the formation of microvessels in mice that underwent implantation; however, the vessel area was notably smaller in the GIOM group. This reduction in vascular area likely reflects the natural progression of regeneration in which early-stage neovascularization, essential for delivering immune cells and stem cells to the defect site, is succeeded by vascular remodeling. Consequently, the lower vascular density in GIOM constructs suggests that the early regeneration phase has completed, resulting in a stabilized microvascular network similar to that observed in the SHAM

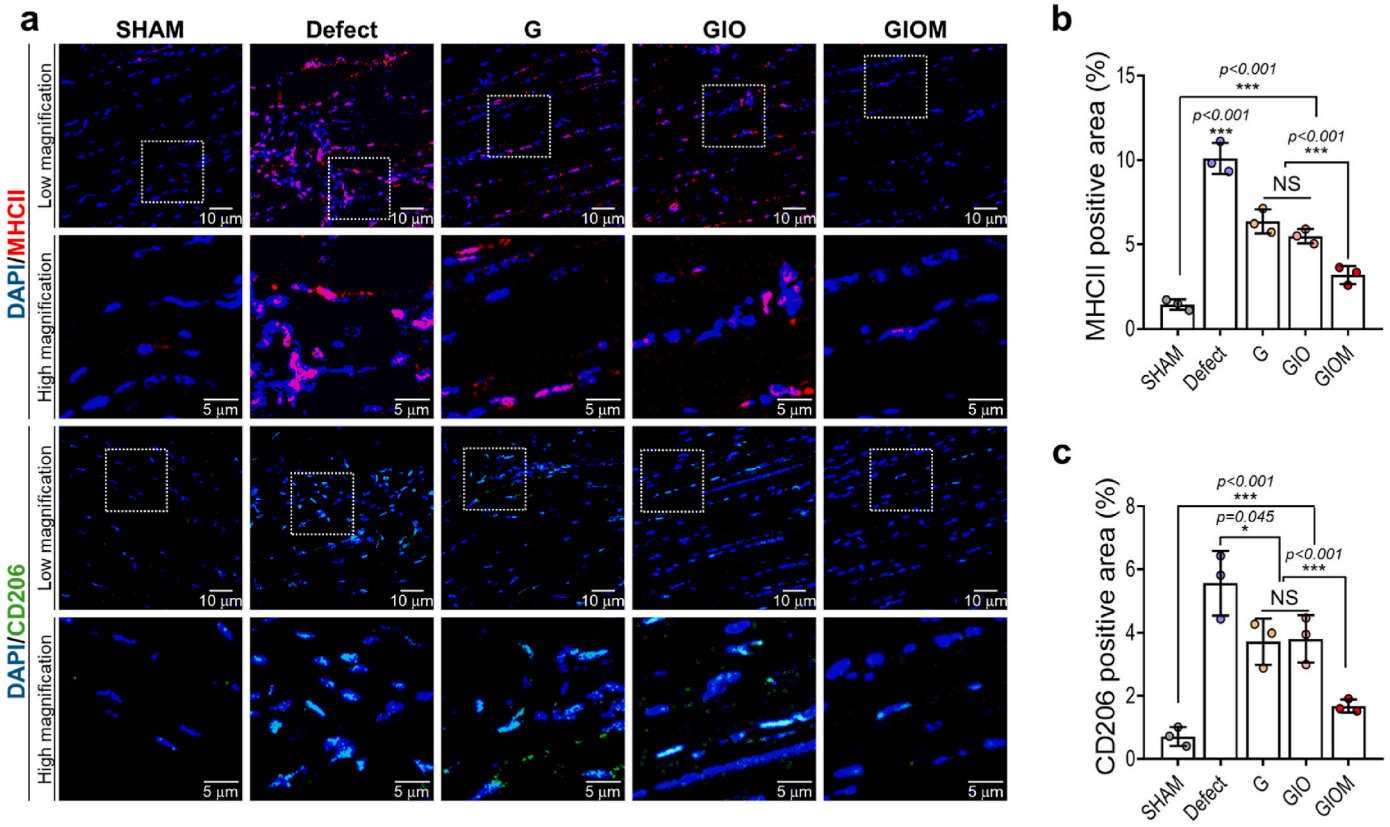

Fig. 9. Immunochemical staining analysis of immune responses. (**a**) Immunochemical staining images of DAPI/MHCII (red) and DAPI/CD206 (green), and quantification of (**b**) MHCII (n = 3, animal number = 3) and (**c**) CD206 (n = 3, animal number = 3) positive areas.

group.

In general, nonbiodegradable nanoparticles can elicit immune responses by persisting in tissues and interacting with immune cells, potentially leading to chronic inflammation or immune activation [46]. Their inability to be efficiently metabolized or cleared may prolong their presence in the body and exacerbate immune reactions [47,48]. Iron oxide nanoparticles generally exhibit low immunogenicity, although their potential to induce immune responses depends on factors such as particle size, concentration, surface characteristics, and the local tissue environment.

Herein, human cells (hASCs) were employed in a VML defect model using C57BL/6 mice to assess the regenerative potential of the GIOM bioconstruct. Although cross-species models often pose risks of immune rejection and inflammation, the C57BL/6 strain is widely used in studies of human-mouse cell interactions due to its immunological robustness [49–51]. To address any potential immune response, we evaluated M1 (MHCII) and M2 (CD206) macrophage marker expression at the defect site. (Fig. 9a). The results indicated that the expression was significantly more pronounced in the defect group and much lower expression of M1 and M2 was observed in the G, GIO, and GIOM groups (Fig. 9b and c, and Supplementary Fig. S12b). In particular, in the GIOM group, the levels of M1 and M2 macrophages were much closer to those in the sham group. While the VML model results alone did not allow us to definitively conclude that the iron oxide nanoparticles used in this study did not significantly affect the immune response, we cautiously inferred that the concentration of these nanoparticles did not influence the immune response in the VML animal model. However, the number of M1 and M2 macrophages varies based on the degree of muscle regeneration.

4. Conclusion

In conclusion, our study demonstrates the potential of *in situ* M-field bioprinting for the fabrication of highly bioactive bioconstructs that could be utilized as therapeutics for VML defects. Through a comprehensive evaluation of the magnet setup and iron oxide particle size, the cellular alignment and myogenic activities of the hASCs were upregulated. The results show the importance of mechanotransduction pathways, including the Hippo signaling pathway and stretch-activated ion channels, in mediating cellular responses to mechanical stress through the movement of iron oxide particles in the presence of an M-field, thereby facilitating muscle regeneration. Additionally, through *in vivo* assessments of the VML defect model in mice, we revealed the beneficial effects of bioconstruct implantation supplemented with M-field stimulation on muscle tissue regeneration. Notably, the incorporation of iron oxide nanoparticles into the bioconstructs did not induce adverse effects, but instead enhanced cellular responses, as evidenced by increased myogenic activities and improved muscle functionalities.

CRediT authorship contribution statement

Hanjun Hwangbo: Writing – original draft, Methodology, Investigation, Conceptualization. **SooJung Chae:** Investigation, Conceptualization. **Dongryeol Ryu:** Methodology. **GeunHyung Kim:** Writing – review & editing, Writing – original draft, Supervision, Methodology, Conceptualization.

Ethics approval and consent to participate

All the protocols for animal experiments were carried out following the approved protocol (GIST-2023-017) of the Animal Care and Use Committee of the Gwangju Institute of Science and Technology (GIST) in South Korea.

Declaration of competing interest

The authors (Hanjun Hwangbo, SooJung Chae, Dongryeol Ryu, GeunHyung Kim) declare that they have no known competing financial interests or personal relationships that could have appeared to influence the work reported in this paper.

Acknowledgements

This research was supported by the 'Korea National Institute of Health' research project (2022ER130502) and a grant from by SMC-SKKU Future Convergence Academic Research Program, 2024. In addition, this work was also supported by the National Research Foundation of Korea (NRF) grant funded by the Korea government (MSIT) (RS-2024-00336758).

Appendix A. Supplementary data

Supplementary data to this article can be found online at https://doi.org/10.1016/j.bioactmat.2024.11.035.

References

[1] P.G. Campbell, L.E. Weiss, Tissue engineering with the aid of inkjet printers, Expet Opin. Biol. Ther. 7 (8) (2007) 1123–1127.
[2] M. Samandari, A. Mostafavi, J. Quint, A. Memić, A. Tamayol, In situ bioprinting: intraoperative implementation of regenerative medicine, Trends Biotechnol. 40 (10) (2022) 1229–1247.
[3] M. Xie, Y. Shi, C. Zhang, M. Ge, J. Zhang, Z. Chen, J. Fu, Z. Xie, Y. He, In situ 3D bioprinting with bioconcrete bioink, Nat. Commun. 13 (1) (2022) 3597.
[4] M. Albanna, K.W. Binder, S.V. Murphy, J. Kim, S.A. Qasem, W. Zhao, J. Tan, I.B. El-Amin, D.D. Dice, J. Marco, In situ bioprinting of autologous skin cells accelerates wound healing of extensive excisional full-thickness wounds, Sci. Rep. 9 (1) (2019) 1856.
[5] S. Lee, W. Kim, G. Kim, Efficient myogenic activities achieved through blade-casting-assisted bioprinting of aligned myoblasts laden in collagen bioink, Biomacromolecules 24 (11) (2023) 5219–5229.
[6] H. Hwangbo, H. Lee, E.J. Jin, Y. Jo, J. Son, H.M. Woo, D. Ryu, G.H. Kim, Photosynthetic Cyanobacteria can clearly Induce efficient muscle tissue regeneration of bioprinted cell-constructs, Adv. Funct. Mater. 33 (10) (2023) 2209157.
[7] W. Kim, H. Lee, C.K. Lee, J.W. Kyung, S.B. An, I.B. Han, G.H. Kim, A bioprinting process supplemented with in situ electrical stimulation directly induces significant myotube formation and myogenesis, Adv. Funct. Mater. 31 (51) (2021) 2105170.
[8] W. Kim, G. Kim, Bioprinting 3D muscle tissue supplemented with endothelial-spheroids for neuromuscular junction model, Appl. Phys. Rev. 10 (3) (2023).
[9] M.R. Love, S. Palee, S.C. Chattipakorn, N. Chattipakorn, Effects of electrical stimulation on cell proliferation and apoptosis, J. Cell. Physiol. 233 (3) (2018) 1860–1876.
[10] M. Samandari, F. Alipanah, K. Majidzadeh-A, M.M. Alvarez, G. Trujillo-de Santiago, A. Tamayol, Controlling cellular organization in bioprinting through designed 3D microcompartmentalization, Appl. Phys. Rev. 8 (2) (2021).
[11] H. Hwangbo, W. Kim, G.H. Kim, Lotus-root-like microchanneled collagen scaffold, ACS Appl. Mater. Interfaces 13 (11) (2020) 12656–12667.
[12] H. Hwangbo, H. Lee, E.J. Roh, W. Kim, H.P. Joshi, S.Y. Kwon, U.Y. Choi, I.-B. Han, G.H. Kim, Bone tissue engineering via application of a collagen/hydroxyapatite 4D-printed biomimetic scaffold for spinal fusion, Appl. Phys. Rev. 8 (2) (2021).
[13] D. Baptista, L. Teixeira, C. van Blitterswijk, S. Giselbrecht, R. Truckenmüller, Overlooked? Underestimated? Effects of substrate curvature on cell behavior, Trends Biotechnol. 37 (8) (2019) 838–854.
[14] H. Hwangbo, H. Lee, E.-J. Jin, J. Lee, Y. Jo, D. Ryu, G. Kim, Bio-printing of aligned GelMa-based cell-laden structure for muscle tissue regeneration, Bioact. Mater. 8 (2022) 57–70.
[15] C. Wu, Y. Shen, M. Chen, K. Wang, Y. Li, Y. Cheng, Recent advances in magnetic-nanomaterial-based mechanotransduction for cell fate regulation, Adv. Mater. 30 (17) (2018) 1705673.
[16] V.W. Wong, K.C. Rustad, S. Akaishi, M. Sorkin, J.P. Glotzbach, M. Januszyk, E. R. Nelson, K. Levi, J. Paterno, I.N. Vial, Focal adhesion kinase links mechanical force to skin fibrosis via inflammatory signaling, Nat. Med. 18 (1) (2012) 148–152.
[17] Z. Sun, S.S. Guo, R. Fässler, Integrin-mediated mechanotransduction, J. Cell Biol. 215 (4) (2016) 445–456.
[18] W. Liu, Q. Sun, Z.L. Zheng, Y.T. Gao, G.Y. Zhu, Q. Wei, J.Z. Xu, Z.M. Li, C.S. Zhao, Topographic cues guiding cell polarization via distinct cellular mechanosensing pathways, Small 18 (2) (2022) 2104328.
[19] L. Wang, T. Li, Z. Wang, J. Hou, S. Liu, Q. Yang, L. Yu, W. Guo, Y. Wang, B. Guo, Injectable remote magnetic nanofiber/hydrogel multiscale scaffold for functional anisotropic skeletal muscle regeneration, Biomaterials 285 (2022) 121537.
[20] W. Dai, L. Zhang, Y. Yu, W. Yan, F. Zhao, Y. Fan, C. Cao, Q. Cai, X. Hu, Y. Ao, 3D bioprinting of heterogeneous constructs providing tissue-specific microenvironment based on host–guest modulated dynamic hydrogel bioink for osteochondral regeneration, Adv. Funct. Mater. 32 (23) (2022) 2200710.
[21] C. Gao, W. Dai, X. Wang, L. Zhang, Y. Wang, Y. Huang, Z. Yuan, X. Zhang, Y. Yu, X. Yang, Magnesium gradient-based hierarchical scaffold for dual-lineage regeneration of osteochondral defect, Adv. Funct. Mater. 33 (43) (2023) 2304829.
[22] S. Zanganeh, G. Hutter, R. Spitler, O. Lenkov, M. Mahmoudi, A. Shaw, J. S. Pajarinen, H. Nejadnik, S. Goodman, M. Moseley, Iron oxide nanoparticles inhibit tumour growth by inducing pro-inflammatory macrophage polarization in tumour tissues, Nat. Nanotechnol. 11 (11) (2016) 986–994.
[23] U.S. Patil, S. Adireddy, A. Jaiswal, S. Mandava, B.R. Lee, D.B. Chrisey, In vitro/in vivo toxicity evaluation and quantification of iron oxide nanoparticles, Int. J. Mol. Sci. 16 (10) (2015) 24417–24450.
[24] Y. Chen, S. Hou, Recent progress in the effect of magnetic iron oxide nanoparticles on cells and extracellular vesicles, Cell Death Dis. 9 (1) (2023) 195.
[25] Z. Yarjanli, K. Ghaedi, A. Esmaeili, S. Rahgozar, A. Zarrabi, Iron oxide nanoparticles may damage to the neural tissue through iron accumulation, oxidative stress, and protein aggregation, BMC Neurosci. 18 (2017) 1–12.
[26] L. Chang, Y. Li, M. Li, S. Liu, J. Han, G. Zhao, C. Ji, Y. Lyu, G.M. Genin, B. Bai, An Injectable, biodegradable magnetic hydrogel system for exogenous promotion of muscle mass and regeneration, Chem. Eng. J. 420 (2021) 130398.
[27] M.D. Nguyen, H.-V. Tran, S. Xu, T.R. Lee, Fe3O4 nanoparticles: structures, synthesis, magnetic properties, surface functionalization, and emerging applications, Appl. Sci. 11 (23) (2021) 11301.
[28] M. Sharrouf, R. Awad, M. Roumie, S. Marhaba, Structural, optical and room temperature magnetic study of Mn 2 O 3 nanoparticles, Mater. Sci. Appl. 6 (10) (2015) 850.
[29] G.M. Al-Senani, N.M. Deraz, O.H. Abd-Elkader, Magnetic and characterization studies of CoO/Co3O4 nanocomposite, Processes 8 (7) (2020) 844.
[30] C.-Y. Kao, T.-L. Lin, Y.-H. Lin, A.K.-X. Lee, S.Y. Ng, T.-H. Huang, T.-T. Hsu, Synergistic effect of static magnetic fields and 3D-printed iron-oxide-nanoparticle-containing calcium silicate/poly-ε-caprolactone scaffolds for bone tissue engineering, Cells 11 (24) (2022) 3967.
[31] L. Zhang, W. Dai, C. Gao, W. Wei, R. Huang, X. Zhang, Y. Yu, X. Yang, Q. Cai, Multileveled hierarchical hydrogel with continuous biophysical and biochemical gradients for enhanced repair of full-thickness osteochondral defect, Adv. Mater. 35 (19) (2023) 2209565.
[32] K. Yue, G. Trujillo-de Santiago, M.M. Alvarez, A. Tamayol, N. Annabi, A. Khademhosseini, Synthesis, properties, and biomedical applications of gelatin methacryloyl (GelMA) hydrogels, Biomaterials 73 (2015) 254–271.
[33] W. Kim, C.H. Jang, G. Kim, Bioprinted hASC-laden structures with cell-differentiation niches for muscle regeneration, Chem. Eng. J. 419 (2021) 129570.
[34] X. Yang, Y.-Y. Tong, Z.-C. Li, D. Liang, Aggregation-induced microgelation: a new approach to prepare gels in solution, Soft Matter 7 (3) (2011) 978–985.
[35] C. Rinaldi, A. Chaves, S. Elborai, X.T. He, M. Zahn, Magnetic fluid rheology and flows, Curr. Opin. Colloid Interface Sci. 10 (3–4) (2005) 141–157.
[36] S. Odenbach, Microstructure and rheology of magnetic hybrid materials, Arch. Appl. Mech. 86 (2016) 269–279.
[37] V.A. Codelia, G. Sun, K.D. Irvine, Regulation of YAP by mechanical strain through Jnk and Hippo signaling, Curr. Biol. 24 (17) (2014) 2012–2017.
[38] V. Rausch, C.G. Hansen, The Hippo pathway, YAP/TAZ, and the plasma membrane, Trends Cell Biol. 30 (1) (2020) 32–48.
[39] K.I. Watt, K.F. Harvey, P. Gregorevic, Regulation of tissue growth by the mammalian Hippo signaling pathway, Front. Physiol. 8 (2017) 942.
[40] C. Zhao, Y. Li, X. Wang, S. Zou, J. Hu, E. Luo, The effect of uniaxial mechanical stretch on Wnt/β-catenin pathway in bone mesenchymal stem cells, J. Craniofac. Surg. 28 (1) (2017) 113–117.
[41] J. Richardson, A. Kotevski, K. Poole, From stretch to deflection: the importance of context in the activation of mammalian, mechanically activated ion channels, FEBS J. 289 (15) (2022) 4447–4469.
[42] Y. Chandorkar, A. Castro Nava, S. Schweizerhof, M. Van Dongen, T. Haraszti, J. Köhler, H. Zhang, R. Windoffer, A. Mourran, M. Möller, Cellular responses to beating hydrogels to investigate mechanotransduction, Nat. Commun. 10 (1) (2019) 4027.
[43] A.H. Lewis, A.F. Cui, M.F. McDonald, J. Grandl, Transduction of repetitive mechanical stimuli by Piezo1 and Piezo2 ion channels, Cell Rep. 19 (12) (2017) 2572–2585.
[44] H. Liu, J. Hu, Q. Zheng, X. Feng, F. Zhan, X. Wang, G. Xu, F. Hua, Piezo1 channels as force sensors in mechanical force-related chronic inflammation, Front. Immunol. 13 (2022) 816149.
[45] J. Gilbert-Honick, W. Grayson, Vascularized and innervated skeletal muscle tissue engineering, Adv. Healthcare Mater. 9 (1) (2020) 1900626.
[46] J.M. Silva, M. Videira, R. Gaspar, V. Préat, H.F. Florindo, Immune system targeting by biodegradable nanoparticles for cancer vaccines, J. Contr. Release 168 (2) (2013) 179–199.
[47] E. Otieno, Y. Huang, N. Li, T. Li, M. Wang, X. Qiu, X. Xiao, Utilization of superparamagnetic iron oxide nanoparticles (SPIONs) as a vector for drug delivery, Appl. Nanosci. 13 (9) (2023) 6191–6216.
[48] Y. Xu, J.A. Sherwood, K.H. Lackey, Y. Qin, Y. Bao, The responses of immune cells to iron oxide nanoparticles, J. Appl. Toxicol. 36 (4) (2016) 543–553.

[49] H.K. Song, D.Y. Hwang, Use of C57BL/6N mice on the variety of immunological researches, Lab Anim Res. 33 (2017) 119–123.
[50] B.M. Sicari, V. Agrawal, B.F. Siu, C.J. Medberry, C.L. Dearth, N.J. Turner, S. F. Badylak, A murine model of volumetric muscle loss and a regenerative medicine approach for tissue replacement, Tissue Eng. Part A 18 (19–20) (2012) 1941–1948.
[51] C. Hu, G. Chiang, A.H.-P. Chan, C. Alcazar, K.H. Nakayama, M. Quarta, T.A. Rando, N.F. Huang, A mouse model of volumetric muscle loss and therapeutic scaffold implantation, Nat. Protoc. (2024) 1–12.